Remote characterization of the 12 January 2020 eruption of Taal Volcano, Philippines, using seismo-acoustic, volcanic lightning, and satellite observations

Anna Perttu*, Volcanic Risk Solutions, Massey University, Private Bag 11 222, Palmerston North, New Zealand, a.perttu@massey.ac.nz
Jelle Assink, R&D Department of Seismology and Acoustics, Royal Netherlands Meteorological Institute (KNMI), De Bilt, Netherlands, jelle.assink@knmi.nl
Alexa R. Van Eaton, U.S. Geological Survey, Cascades Volcano Observatory, Vancouver, Washington, USA, avaneaton@usgs.gov
Corentin Caudron, Université Libre de Bruxelles, corentin.caudron@ulb.be
Chris Vagasky, Vaisala Inc, chris.vagasky@vaisala.com
Janine Krippner, University of Waikato, jkrippne@waikato.ac.nz
Kathleen McKee, University of Maryland Baltimore County and NASA Goddard Space Flight Center, kfmckee@alaska.edu
Silvio De Angelis, School of Environmental Sciences, University of Liverpool, UK, and Istituto Nazionale di Geofisica e Vulcanologia, Sezione di Pisa, Italy S.De-Angelis@liverpool.ac.uk
Brian Perttu, Volcanic Risk Solutions, Massey University, b.perttu@massey.ac.nz
Benoit Taisne, Earth Observatory of Singapore, Nanyang Technological University, btaisne@ntu.edu.sg
Gert Lube, Volcanic Risk Solutions, Massey University, g.lube@massey.ac.nz

- Corresponding Author: Anna Perttu a.perttu@massey.ac.nz

Key Points

- We distinguish five eruption phases using data from long-range lightning, infrasound, satellite, and seismic sensors.
- Results suggest water from the Main Crater Lake was vaporized and incorporated into the plume within the first 12 hours of the eruption.
- Remote observations can augment local measurements to provide additional details about the eruption dynamics.

Abstract

On 12 January 2020, an eruption began on the shores of the Main Crater Lake of Taal Volcano, a caldera system on the southern end of Luzon Island in the Philippines. Taal, one of the most active volcanoes in the Philippines, is located 30 km south of Manila, a major metropolitan area with a population of 13.5 million people. Eruptive activity intensified throughout the day on 12 January, producing prolific volcanic lightning, ashfall, and a sustained plume that reached 16-17 km altitude. The chronology of events was well documented by the Philippine Institute of Volcanology and Seismology (PHIVOLCS) and the Tokyo Volcanic Ash Advisory Center (VAAC). The wealth of data collected during the eruption provides a unique opportunity to investigate how the combination of different remote sensing methods may complement local observations and monitoring. Remote systems tend to provide lower-resolution data but are also less likely to be compromised by the eruptive activity, thus providing continuous records of eruptive processes. Here, we present a post-event analysis of the 12 January activity, including data from long-range lightning, infrasound, and seismic arrays located at distances up to several thousands of kilometers from the volcano. By combining these datasets we distinguish five phases of activity and infer a major shift in eruption behavior around 12:00 on 12 January (UTC). The remote observations suggest that the most of the water within the Main Crater Lake (~42 million m^3) was vaporized and incorporated into the volcanic plume within the first 12 hours of the eruption.

Introduction

Taal Volcano, located on the southern end of Luzon Island (Figure 1), is one of the most active volcanoes in the Philippines (Delos Reyes et al., 2018; Global Volcanism Program, 2020). This caldera system is located 30 km south of the southern end of the major metropolitan area of Manila, home to 13.5 million people (Philippine Statistics Authority, 2021). The caldera contains Taal Lake (TL) with Taal Volcano Island (TVI) near the center, which itself contains a smaller crater lake known as the Main Crater Lake (MCL). Prior to the 2020 eruption the MCL had a volume of 42 million m^3, a maximum depth of 70 m, a pH of ~3.1, and a usual temperature of ~32° C (Bernard et al., 2020). Both the shores of LT and TVI are populated areas. Taal Volcano poses a hazard not only to the local population but also to more distal communities and the global aviation industry (Delos Reyes et al., 2018).

On 12 January 2020 an eruption began on TVI along the NE shore of the inner lake (MCL) (PHIVOLCS, 2020a; PHIVOLCS-DOST [@phivolcs_dost], 2020a). This study is focused on eruption processes leading to the high-altitude plume on the first day of the eruption, 12 January. This plume impacted aviation, leading to the cancellation of over 240 flights and the closure of Manila's Ninoy Aquino International Airport (Chen, 2020; Reuters, 2020). Twenty-three cities/municipalities experienced power interruption in the provinces of Cavite, Laguna, and Batangas (Santos et al., 2022), and thousands were evacuated, including 142 families who remain displaced at the time of writing (Abanto, 2023).

We use four remotely detected datasets to characterize the volcanic plume during this eruption, including satellite-based imagery (optical and infrared), lightning flashes, and infrasound and seismic waveforms. Each of these technologies have their own pros and cons. Satellite-based remote sensing can allow rapid assessment of the location and height of a volcanic plume, providing information for ash dispersion models; however, satellite observations can be affected by slow data availability (dependent on factors such as scanning strategy and data sharing agreements), spatial resolution, latency, cloudy weather, and nighttime conditions (Poland et al., 2020). Infrasound and lightning detection are independent of time of day and cloud cover, but regional to remote infrasound can suffer from low signal-to-noise ratios (SNR) in strong wind conditions both locally and along the propagation path. Other acoustic signals such as microbaroms from ocean waves can mask the signal of interest (e.g., den Ouden et al., 2020). Moreover, the long-range transmission of acoustic energy from source to sensor is determined by variable atmospheric conditions along the propagation path (e.g., Waxler and Assink, 2019). Long-range lightning detection can be used to identify the presence of an energetic plume and track its location, but it can be challenging to discriminate volcanic lightning from background meteorological storms. In the case of the Taal eruption, the lack of nearby thunderstorms meant this was not a significant issue within 200 km of the volcano (Van Eaton et al., 2022). Compared to local seismic stations (within 20 km), regional seismic arrays are not as sensitive to smaller amplitude seismicity near the volcano and benefit from the improvement of the signal-to-noise ratio (SNR) through array processing techniques to detect activity from a greater distance where they are less likely to be directly impacted by the eruption. SNR is enhanced through beamforming, the combination of different elements within the array such that coherent signal is amplified and the noncoherent noise is reduced. Similar to infrasonic arrays, which are impacted by the microbarom and other noise sources, concurrent seismic signals, such as microseisms in the 0.1–1.0 Hz band and anthropogenic noise at higher frequencies, may mask the signals of interest. Combined, these four tools help compensate for their individual limitations and offer an effective way to assess volcanic eruptions and their dynamics (e.g., Coombs et al., 2018).

Here, we investigate data from regional and remote monitoring networks to explore how their synthesis may complement local observations. Throughout this paper, we use hours:minutes:seconds for higher resolution data and hours:minutes for lower-resolution data. All times are reported in UTC unless noted, with an 8-hour time difference between UTC and Philippine Standard Time (UTC +8). A list of abbreviations is available in table S1.

Eruption Timeline Determined by Local Sources

An eruption timeline was constructed using a variety of sources including bulletins and social media posts from the Philippine Institute of Volcanology and Seismology (PHIVOLCS) and the Tokyo Volcanic Ash Advisory Center (Tokyo VAAC) (Figure 2, supplemental Table S2 and supplemental Figure S1). These observations were combined with photographs and videos from social media (Twitter and Instagram), Getty Images, and news sources that provided estimated acquisition times (Table S3). The Tokyo VAAC reports are based on information from the Japan Meteorological Agency's Himawari-8 satellite, as well as observations from PHIVOLCS, and the Air Traffic Service within the Manila Flight Information Region (FIR). There was a wide range of social media and traditional media postings with video and photographs of the eruption however, most lacked information on time and location. We inferred locations by comparing images to those with known locations, such as a webcam operated by PHIVOLCS, and by identifying recognizable features within the frame. Plume heights are reported above sea level (a.s.l.) unless otherwise noted. All information from PHIVOLCS and VAAC alerts and bulletins are listed in Table S2 and summarized below.

An initial swarm of earthquakes was detected beginning around 03:00 UTC (DOST-PHIVOLCS, 2021) and was also felt and reported by the local population in the area near the future eruption site (Martinez-Villegas et al., 2022). Based on visual observations, explosive activity began around 05:00 on 12 January 2020, with small phreatic (steam) explosions, producing plumes up to 100 m high within the Main Crater Lake (Figure 1, PHIVOLCS, 2020b). This activity was recorded by the webcam operated by PHIVOLCS (PHIVOLCS-DOST [@phivolcs_dost], 2020b) and video footage posted on social media platforms (Adrian [SaiAdrian], 2020). The explosions originated from a known hydrothermal area with at least five observed steam vents (Global Volcanism Program, 2020). A tourist guide present at the Main Crater Rim overlook at approximately 04:30 stated that they saw a fissure form within the crater, that steaming became stronger, and that it was coming from a big hole before "it cracked open" (Martinez-Villegas et al., 2022). The activity observed onshore in the

PHIVOLCS TVI webcam migrated toward the lake at 05:40, became increasingly energetic at 06:00, as indicated by larger plumes, and at 06:15 the camera lens was obscured and ultimately damaged by the growing eruption (Martinez-Villegas et al., 2022). Between 06:34 and 06:40 Martinez-Villegas et al. (2022) reported that based on PHIVOLCS web camera images, the eruption transitioned to phreatomagmatic activity.

This observation was followed by an escalation of activity; a 1.5 km plume was observed in satellite data and reported by the VAAC at 07:01 (Tokyo VAAC, 2020). A video posted online at 07:09 (Table S3) showed a much higher-altitude plume that appeared light in color. A time-lapse video posted at 09:26 showed the plume growing from a smaller radius to filling the MCL area. Several distinct explosions can be seen in the time-lapse. By 09:30 both the Tokyo VAAC and PHIVOLCS reported a high-altitude plume to 15-17 km producing frequent lightning (PHIVOLCS, 2020c; Tokyo VAAC, 2020). At around sunset (before 09:44) video footage from two separate locations (Tagaytay area NNW of TVI, and the Balet area east of TVI) showed two plumes: one large, higher-altitude, light-colored (possibly more steam-rich) plume to the south, and a second significantly lower, darker (possibly more ash-rich) plume to the northeast. From both of these locations the shorter, darker plume appeared to originate from the NNE corner of the MCL area, where PHIVOLCS webcam images indicated the location of the initial eruptive activity (Table S3). The large, lighter-colored plume took up the majority of the MCL area. An observer indicated that by 14:00 PST (06:00 UTC) “it was already big” and around 15:00 PST (07:00 UTC) “the ash [column] was already huge” (Martinez-Villegas, M. 2020). Several eyewitnesses also reported that between 06:00–08:00, there was wet ash fall, and some described it as mud (Martinez-Villegas et al., 2022). Local sunset was around 18:44 PST (09:44 UTC). A few more images capturing lightning within the plume were taken at local evening time (Table S3).

The plume top eventually reached 15–17 km and was reported by both PHIVOLCS and the VAAC to be sustained for several hours. While there was a gap in webcam visibility of the eruption due to heavy ash fall and electricity outages, an image was taken with a camera and shared at 17:59 from Escala - Tagaytay (PHIVOLCS, personal communication 14 October 2022). PHIVOLCS reported a shift in activity at 18:40 to a magmatic eruption “characterized by weak lava fountaining accompanied by thunder and flashes of lightning” as the “lake water in the Main Crater completely vaporized” (PHIVOLCS, 2020d; DOST-PHIVOLCS, 2021). Images were posted online from both PHIVOLCS and local photographers, showing incandescent material that was visible to the naked eye (PHIVOLCS-DOST [@phivolcs_dost], 2020c; Quiambao, P., personal communication 27 August 2022). Eyewitnesses reported feeling explosions between 18:00–19:00 (Martinez-Villegas et al., 2022). At 23:20 the Tokyo VAAC reported that the high-level plume, up to 17 km, had detached from the vent and there was a lower altitude plume rising up to 11 km from the vent (Tokyo VAAC, 2020). By 02:20 on 13 January all observed plumes had detached from the vent and were partially obscured by meteorologic cloud cover (Tokyo VAAC, 2020). At 14:20 on 13 January the VAAC reported that the ash had dissipated and was no longer observable by the Himawari-8 satellite.

Although there was no longer a significant ash plume being generated, activity at the vent continued at a lower intensity. Throughout 13 and 14 January PHIVOLCS reported lava fountaining and “steam rich plumes” to various heights not exceeding 2 km. (PHIVOLCS, 2020e, 2020f). On 15 January PHIVOLCS reported a continuous, but generally weaker, eruption with dark gray, steam-laden plumes to 1 km. (PHIVOLCS, 2020g). Between 16–21 January, PHIVOLCS reported plumes fluctuating between 500–800 m (PHIVOLCS, 2020h, 2020i, 2020j, 2020k, 2020l, 2020 m, 2020n). By 22 January, the activity was limited to steam plumes 50–500 m high within the vent area, and an advisory at 16:00 PST local time stated that since 05:00 PST there had been no ash emissions and that ashfall was due to remobilized ash (PHIVOLCS, 2020n). The eruption from 12–17 January was accompanied by a dike intrusion. Bato et al. (2021) modeled the intrusion as a 21 x 8 km, near-vertical, NE-striking dike under TVI that produced NE-SW ground fissures in several communities (PHIVOLCS, 2020o). It was first discerned in the “co-eruptive” SAR data between 9–17 January (Bato et al., 2021).

This near real-time chronology exemplifies the challenges of providing continuous data using local monitoring networks, as the majority of monitoring stations on TVI were either destroyed or disrupted, and solar panels powering the wider network were covered with ash, which disrupted the data transmission. PHIVOLCS reported that, of the five seismic stations on TVI, only one was still functioning and able to send data after the initial activity on 12 January (Sabillo, 2020). PHIVOLCS also reported issues with ash covering the solar panels and power issues at seismic stations around TL; they were using the Philippine National Seismic Network and were working to clear panels, as well as setting up new stations in the aftermath of the eruption (Sabillo, 2020; Sabillo [@kristinesabillo], 2020).

Due to the proximity of this eruption to major population centers, it was possible to crowdsource ash samples and footage of the eruption. Balangue-Tarriela et al. (2022) took advantage of this information to examine the tephra deposits around the volcano in the region known as CALABARZON (Cavite, Laguna, Batangas, Rizal, and Quezon) and the Metro Manila area. Their results confirm that the eruption was phreatomagmatic, based on the presence of abundant accretionary lapilli (wet clumps of ash), overall fine-grained, lithic-rich deposits, and ubiquitous hackle lines and stepped features on the ash grain surfaces, which are indicative of magma-water interaction (Balangue-Tarriela et al., 2022). They noted four stratigraphic layers consisting of a basal, light gray ash (layer 1), dark gray ash and lapilli (layer 2), brown ash (layer 3, the thickest unit), and an uppermost light gray ash (layer 4). Their volume for the total fall deposit ranged from 0.04 to 0.10 km^3 (bulk) using a range of volume-fitting assumptions. This bulk eruptive volume is on the low end of the estimate from Van Eaton et al. (2022) (0.1–0.9 km^3), which was based on plume heights alone.

Satellite Datasets

We assessed a wide range of satellite observations for coverage of the event, but due to spatial and temporal gaps in coverage there were limited syn-eruptive scenes acquired. Aqua, Terra, Sentinel-2, Suomi NPP (Visible Infrared Imaging Radiometer Suite or VIIRS sensor), and NOAA-20 (VIIRS sensor) satellites each only had one overpass during the eruption, while Sentinel-5/TROPOMI had two overpasses (Figure 3, Figure S2, Table S4). Ambient cloud cover further reduced the number of scenes that could be used for observation of the eruption. The Japan Meteorological Agency's geostationary Himawari-8 satellite was the most successful in imaging the eruption, with 288 scenes acquired at 10-minute intervals from 12–13 January (Figure 3). We used the plume heights from Van Eaton et al. (2022), which were determined from Himawari-8 thermal infrared brightness temperatures in the 11 micron channel. Their single coldest pixel within 30 km of Taal Volcano was matched to atmospheric temperature profiles from Reanalysis-1 model output at 6-hourly intervals (Figure 3). We used the corrected satellite times to account for the time of the actual overpass over Taal Volcano, which occurred 3 min later than the scan start of each image (Van Eaton et al., 2022). We performed an additional qualitative analysis of the Himawari-8 infrared observations to identify discrete eruptive "pulses." A pulse was defined by a short-lived (minutes-long) increase in plume height, indicating a possible increase in eruption rate at the vent. Pulses were identified by comparing plume heights in individual images with those in images taken immediately before or after—i.e., 10 minutes earlier or later.

The Himawari-8 visible and infrared images (Bachmeier, 2020) showed an ash plume rising above the surrounding meteorologic clouds by 06:33 UTC and establishing a sustained umbrella region by 07:43. The umbrella continues expanding steadily until ~10:03, after which it begins to recede in the upwind direction (Van Eaton et al., 2022). Renewed upwind expansion are observed by ~11:03 and remains relatively stable until recession and weakening by 12:03. There is an eruptive pulse identifiable at 12:43, and then the plume weakens again at 13:13. The plume loses its umbrella-like morphology ~14:03 and then begins a phase of pulsatory eruptive behavior with several pauses in activity. Discrete eruptive pulses are observed at 14:03, 14:33, 15:03, 15:23, 15:53, 16:03, 16:23, 16:53, 17:13, and 17:33. After 17:33, the plume detaches from the vent and disperses downwind. The plume is no longer clearly identifiable near the volcano after 20:23.

Volcanic lightning

Volcanic lightning data from Vaisala's Global Lightning Dataset (GLD360) were reported by Van Eaton et al. (2022). The GLD360 network employs both time-of-arrival and magnetic direction-finding technologies to geolocate individual lightning strokes, which can then be grouped into flashes (Said et al., 2010). The sensors in the GLD360 network are sensitive to the very low frequency range (500 Hz–50 kHz) and use a waveform recognition algorithm to identify specific features in the radio waves generated by each lightning stroke. A central processor combines measurements from multiple sensors to calculate the time and location of each stroke, classifies whether the stroke was cloud-to-cloud or cloud-to-ground, and determines the polarity and effective peak current.

Van Eaton et al. (2022) reported that volcanic lightning was not detected until Taal's plume exceeded 10 km. Their explanation was that the lower-level plume was too warm to nucleate ice, which is needed to create abundant, high-energy lightning detectable by global networks. It is also plausible that the incorporation of surface water into the plume helped create a mixed-phase microphysical region in the upper plume (i.e., containing supercooled liquid water, ice, and graupel), which greatly intensified the lightning activity (Van Eaton et al., 2022).

Analyzing the volcanic lightning flashes reported by Van Eaton et al. (2022) in greater detail for this study, we have defined several stages of activity with varying flash rates (Lightning Stages A through E; Figure 4). We delineated proximal, distal, and total lightning rates, which can be useful to identify lighting associated with an actively erupting plume rather than drifting, electrified ash (cf. Van Eaton et al., 2016). Proximal lightning was defined as occurring within 20 km of the vent, and distal lightning from 20–200 km. Lightning Stage A from 07:03 to 08:16 UTC is defined by moderate flash rates, with an average of ~4 flashes min^{-1} in the proximal zone, and distal lightning <= 1 flash min^{-1}. Lightning Stage B from 08:16 to 10:30 is characterized by a rapid increase then steadying of flash rates, to a steady rate of ~26 total flashes min^{-1} on average (76% of which occur in proximal zone <20 km from vent). Lightning Stage C from 10:30 to 15:40 shows a consistently high but fluctuating flash rate with an average of 44 flashes min^{-1} and a maximum of 85 flashes min^{-1} (54% of which occur in the proximal zone). Lightning Stage D from 15:40 to 17:36 shows an average of 12 flashes min^{-1} and a maximum of 31 flashes min^{-1} (87% of which occur in the proximal zone). Lightning Stage E from 17:36 to 20:27 shows another reduction in flash rate to less than 3 total flashes min^{-1} (entirely in the proximal zone) before ending completely by 20:27.

Infrasound

The eruption on 12 January generated infrasound (i.e., low-frequency sound below 20 Hz) that was recorded on various infrasound arrays, including many that are part of the International Monitoring System (IMS), as well as one in Singapore (SING). The closest array to Taal is the I39PW array, located 1,645 km southeast in Palau. The next closest station is the SING array in Singapore, located 2,350 km southwest (Table S5). The Taal eruption had good azimuthal coverage in terms of remote IMS and non-IMS arrays (Figure 1).

We used several array processing techniques to process the infrasound data and to characterize the recorded signals. In order to identify the signal generated by Taal on the regional infrasound network, we used the Progressive Multi-Channel Correlation (PMCC) algorithm (Cansi, 1995) with the IMS standard filters also used by Matoza et al. (2013) (Figure 5). The eruption was strongly detected by remote infrasound arrays: I39PW (Palau) and I30JP (Japan), and detected at I07AU (Central Australia), SING (Singapore), I34MN (Mongolia), and I44RU (Kamchatka Russia). I06AU (Cocos Islands) has a marginal detection and is therefore not included, I40PG (Papua New Guinea) had data quality issues at the time, and while it appears to have detected the event, the array processing is not reliable. The best time series with the most details was recorded at the Palau I39PW station. For array processing results from other stations please see Figures S4-S9.

The observations at the nearest IMS array I39PW are further analyzed using time-domain (Melton and Bailey, 1957) and frequency-domain (Smart and Flinn, 1971) Fisher detector techniques. These detectors rely on the evaluation of the Fisher ratio, which corresponds to the probability of detection of a signal with a threshold signal-to-noise ratio (SNR) or greater. We processed the detrended data in a frequency band between 0.07 and 1 Hz using 60-second windows with a 90% overlap. For each time-bin, the Fisher ratio is evaluated over a two-dimensional slowness grid that is parameterized by back azimuth values between 280-320 degrees and apparent velocity values between 300-450 m/s. Back azimuth values and apparent velocity values are spaced by 0.5 degrees and 2.5 m/s, respectively. The slowness that maximizes Fisher-ratio in each time bin is used to compute the best-beam as well as the Power Spectral Density (PSD) and SNR spectrograms (Figures 6a and 6b). The estimated plane-wave parameters are aggregated in 10-minute time-bins (Figures 6d and 6e). Only time-bins with at least two detections are considered. The back-azimuth and apparent velocity bins widths are 1 degree and 5 m/s, respectively. We examined the peak frequency through time (Figure S10) following the methods shown in McKee et al. (2021a) and McKee et al. (2021b) for the closest array, I39PW.

I39PW Palau Infrasound Array Results

Array processing results place the beginning of coherent regional infrasound at I39PW at 08:30 on 12 January (Figure 6). Note that the times in the following text and Figure 6 have been approximately corrected for the propagation time to the array, by considering a celerity (distance / travel time) of 0.26 km/s (see section Infrasound Propagation Modeling). It follows that the latest Taal became acoustically active was around 06:45:30. Between approximately 07:00-12:00 a low-frequency signal was observed with a frequency content between 0.02-0.2 Hz. For the first part of the detection, the lowest frequencies are partly masked by wind noise; the progressive improvement in detectability between 07:00-08:00 is likely related to the transition toward a stable boundary layer at the station, reducing noise generated by turbulence (Smink et al., 2019, Perttu et al., 2020a). After 12:00 higher frequency signals (0.5-3 Hz) become present in the array processing results. We note in particular the high-frequency signals between 13:12-14:27. Infrasound detections ended by 20:06, with a few sporadic detections through 13 January. The detections have high coherency through ~14:15, after which the coherency decreases. The continuous background noise spectrum of microbarom signals (0.2-0.8 Hz) are clearly present in the spectrograms (Figure 6a and 6b). This is to be expected as I39PW is an island array. We also computed the peak frequency (frequency associated with peak power) through time of the beamform (Figure S10). The peak frequency is between 0.08 to 0.1 Hz from 06:45 - 10:45, after which it steadily transitions to between 0.18 and 0.23 Hz, with a maximum frequency of 0.27 Hz at 19:10. As the peak frequency increases the spectral curve narrows, reflecting a loss of lower frequency signal through time. There is potentially interference with other non-volcanic signals in the later period of the signal as the SNR decreases.

We calculated acoustic power following the method presented in Perttu et al. (2020b). The acoustic power for the Taal eruption peaks at $2.90x10^7$ W at 08:14 (Figure S11). This is associated with the very low frequency infrasound signal. There is a second peak in acoustic power of $7.22x10^6$ W at 13:44 associated with the higher frequencies recorded later in the eruption.

Infrasound Propagation modeling

In order to interpret the remote infrasound observations of Taal in terms of the source processes, it is important to quantify the long-range propagation characteristics using infrasound propagation models. As infrasound propagates throughout the atmosphere, it is sensitive to spatio-temporal variations in temperature and wind (e.g., Smets et al., 2016; Assink et al., 2019). The effective sound speed c_{eff} approximates the refractive effects of temperature and wind gradients (Assink et al., 2017), and is defined as the adiabatic sound speed (a function of temperature *T*) plus the horizontal wind *u* in the direction of propagation *n*: $c_{eff} \sim 20\sqrt{T} + u \cdot n$. In order to quantify ground-to-ground ducting efficiency, it is helpful to introduce the effective sound speed ratio, c_{eff} ratio, which is defined as the effective sound speed normalized by its value on the ground. Efficient ground-to-ground ducting conditions are expected for c_{eff} ratio values exceeding unity.

Figure 7 shows effective sound speed ratio profiles and infrasound propagation results for the path from Taal to I39PW. The c_{eff} ratio profiles are computed using the Ground-to-Space (G2S) atmospheric model (Drob, 2019). This model is compiled from operational numerical weather prediction model specifications by the National Oceanic and Atmospheric Administration (NOAA) and the National Aeronautics and Space Administration (NASA) for the lower and middle atmosphere. Above the stratopause, the Horizontal Wind Model (HWM) and The Mass Spectrometer Incoherent Scatter radar (MSIS) semi-empirical models are used. The G2S model is available for each hour of the day and is interpolated to a 0.5x0.5 degrees spatial grid. From the effective sound speed ratio profiles, it can be concluded that there is a borderline stratospheric duct toward the array. A thermospheric duct between the ground and ~120 km altitude is always present, because of the large temperature gradient in the lower thermosphere (Figures S12 and S13).

Propagation toward I39PW has been computed using the *ePape* Parabolic Equation (PE) model (Waxler et al., 2021; 2022) and the *InfraGA* raytracer (Blom, 2019). The PE model is a full-wave model, cast in cartesian coordinates, and takes lateral variations in temperature and wind along the propagation path into account. Out-of-plane propagation effects are not included. The ray theoretical model is a geometric approximation to the wave-equation and does not include full-wave effects. The model is cast in spherical coordinates and traces rays through the full 3D atmospheric model space. For both models the effects of absorption (Sutherland and Bass, 2004) are included. For this study, ray theory is used to find the eigenrays that connect Taal to I39PW. For each eigenray, traveltime, back azimuth deviation, and apparent velocity (e.g., Smets et al., 2016) is obtained. The PE is used to estimate the transmission loss toward I39PW.

Figure 7 shows propagation results for 09:00 UTC on 12 January 2020. The PE field is computed at 0.1 Hz and is presented as transmission loss as a function of range and altitude. The range-altitude plane shows that infrasound is guided in both stratospheric and thermospheric waveguides. However, along the path the stratospheric duct weakens significantly (Figure S12) and vanishes towards I39PW. The thermospheric duct remains present along the entire path. From the ground transmission loss curve (bottom panel), it follows that the transmission loss at I39PW is 56.5 dB (re 1 km) at 0.1 Hz, assuming a point source.

Using 3D ray tracing, two thermospheric eigenrays are identified for 09:00 UTC (Table 1). The fastest eigenray arrives with a celerity of ~260 m/s. The computed back azimuth (298 degrees) and apparent velocity (~348 m/s) values match the observations well (Figures 6d and 6e). A good agreement is noted for other model times as well, with exception of the arrival branch with higher apparent velocities. Notably, these rays reach higher in the thermosphere and are more susceptible to atmospheric absorption and therefore possibly not observable. The celerities of the eigenrays between Taal and I39PW vary throughout the day between 259-265 m/s, due to the effects of the semi-diurnal tides (Assink et al., 2012; see Figure S14). In addition, we note that the borderline stratospheric duct strengthens throughout the day (compare Figure S12 to S13). This leads to the simulation of stratospheric eigenrays at 22:00 UTC (Figure S14), after the main eruption phase has finished.

Seismic Observations

To characterize the seismicity associated with the eruption, we analyzed data from one local seismic station, Tagaytay (TGY), which is part of the auxiliary seismic network of the IMS. This station consists of an STS-2 three-component seismometer and is situated 11 km from the Taal Main Crater Lake (MCL). We also used remote seismic arrays CMAR (Chiang Mai, Thailand; 2404 km), SONM (Songino, Mongolia; 3987 km), WRA (Warramunga, Australia; 4032 km), ASAR (Alice Springs, Australia; 4400 km) and MKAR (Makanchi, Kazakhstan; 5109 km) that are positioned around Taal (Figure 1).

On 12 January 2020 after 03:00 at TGY, significant perturbations were measured that can be associated with the eruption (Figure 8). Between 16:45-17:15 a brief data gap for the vertical channel is noted. After 17:15, no data were registered for the horizontal components (Figure S15), possibly because the sensor booms were out of balance following the eruption. In addition to the volcano-tectonic (VT) signals associated with the eruption there were two distinct tremor signals. One is interpreted to be a seismic tremor (TS), while the other is an acoustic tremor (TA) that was coupled into the ground locally and recorded at TGY (cf. Caudron et al., 2015) as discussed in Seismic and Seismo-Acoustic Observations.

Between 03:00 and 06:00, multiple VTs are detected that are indicative of the start of the eruption (Figure S17). Directly following this interval, the seismic registrations show near-continuous tremor as well as individual short-lived pulses. The tremor is characterized by discrete spectral bands. Beginning at 06:09 a continuous tremor signal begins at TGY (TS), mostly between 0.2–4Hz. This signal has some higher frequencies that begin after 08:30 and strongly continues throughout the entire day of 12 January. This tremor signal is present in the horizontal as well as vertical channels (Figure S16). Operational Real-Time Seismic Amplitude Measurement (RSAM) (Endo and Murray, 1991) calculations between 0.1–15 Hz show a clear increase from 03:15 through 08:20 before leveling out at the higher level for the rest of the day (Figure 9).

Between 07:00 and 12:00, a continuous low-frequency tremor signal TA (with energy 0.03–0.2 Hz) is detected on the vertical channel (Figure 8). The amplitude gradually increases, peaks around 08:30, then decreases. This TA signal corresponds to the low-frequency signal detected at I39PW as well as the more distant infrasound arrays. Contrary to other tremor associated with magma-water interaction, this long-lasting signal is not made up of self-similar low-frequency earthquakes (Perttu et al., 2020a; Matoza and Roman, 2022).

The remote seismic arrays positioned around Taal Volcano also picked up the activity on 12-13 January. Here, we discuss the array processing results from CMAR (Figure S18), which provided the best SNR. The results for the more distant arrays can be found in Figures S18–S22. The vertical velocity data are processed using the same time-domain Fisher processing algorithm that was also used for the processing of the I39PW infrasound data (Melton and Bailey, 1957). The CMAR data were bandpass filtered between 0.7–1.8 Hz and processed in 10 second windows with 90% overlap. It follows from spectral analysis that this passband is optimal to avoid microseisms and anthropogenic noise near the CMAR station. Similar passband selection parameters to CMAR were used at other seismic stations, with slight variations to account for different local seismic noise profiles. The two-dimensional slowness grid that was used in the processing of the seismic array data was spanned by a back azimuth cone centered around the theoretical back azimuth to Taal Volcano with a width of 30 degrees, and an apparent velocity range between 2–20 km/s, with steps of 0.5 degrees and 0.2 km/s, respectively.

The array processing results (Figure 10) show a significant increase in high SNR signals from the direction of Taal. The signals consist of short-lived pulses that are detected throughout 12–14 January 2020 with the highest number of detections arriving between 12:00 UTC on 12 January and 00:00 UTC on 13 January. In addition to the short-lived pulses, spectral banding between 0.7–1.5 Hz is apparent. These characteristics are similar to the VT and TS tremor signals observed at station TGY. In fact, individual transient arrivals appear to be well-correlated between stations TGY and CMAR (Figure 11).

There is a notable difference between the theoretical back azimuth to Taal (blue-green line in Figure 10d) and the observed values in the 0.7–1.8 Hz band. The measured apparent velocities of ~14 km/s indicate that these signals correspond to P-wave arrivals with steeper incidence angles. We estimate an incidence angle of 30 degrees with the vertical, given the crustal P-wave speed of 6 km/s (Laske et al., 2013). In contrast, when processing the CMAR data in a lower frequency band of 0.03–0.1 Hz (Figure S20), the azimuthal discrepancy disappears. The apparent velocities of those arrivals are around ~3 km/s, indicating that these are Rayleigh waves. It is known that the Mohorovicic -discontinuity under CMAR strongly refracts arrivals with steep incident angles such as P-waves, affecting the measured slowness values (Flanagan et al., 2012). This process provides a plausible explanation for our observations.

Discussion

The timely interpretation of data during an eruption is key for mitigating the hazards to local communities and international air traffic alike. Given the significant technological advances over the past decade, there is ample scope to augment real-time volcano monitoring with remote methods (e.g., Poland et al., 2020, and references therein). During the 2020 eruption of Taal, the local monitoring network experienced outages in several stations due to the direct impacts of ash fall and destruction of near-vent sensors, as well as indirect effects from power grid outages. This loss of in situ monitoring equipment is not uncommon during major eruptions and highlights the value of complementing local networks with remote methods in an ongoing volcanic crisis. In the following sections, we examine how our remote observations improve the understanding of Taal's eruptive processes in post-analysis and consider how these datasets might be incorporated into a near real-time monitoring framework.

Seismic and Seismo-Acoustic Observations

Figure 8 shows the measured vertical velocities and the associated spectrogram for seismic station TGY. Between 07:00–12:00, a continuous low-frequency signal is detected on the vertical channel that is similar to the observations at the infrasound arrays (TA; Figures 6 and 8). Figure 8 shows that the onset time and duration is consistent with the observations at infrasound array I39PW when considering an infrasonic propagation speed of 0.26 km/s (see Infrasound Propagation Modeling). The low-frequency signal is absent on the horizontal channels as well as other seismic stations within a radius of ~2,000 km around Taal Volcano. This suggests that the observation at TGY is due to acoustic-seismic coupling (i.e. ground coupled airwaves) (Matoza et al., 2019; Bishop et al., 2022; and references therein). At longer ranges, the amplitude of the signal is likely too small to couple to seismometers.

To test the possibility that the TA seismo-acoustic signal from 07:00–12:00 was due to acoustic-seismic coupling, we compare two pressure estimates at station TGY. The first estimate is calculated from the Root Mean Square (RMS) vertical velocity measured at TGY, by using the relationship for seismo-acoustic coupling from Anthony et al. (2022) to calculate the expected amplitude of the acoustic signal required to generate it. The second estimate is calculated from the RMS pressure measured at I39PW, by correcting for the difference in transmission loss at 0.1 Hz between 11 km (TGY) and 1645 km (I39PW). Using the beamform calculated for I39PW, filtered into the range of the signal from 0.05–0.15 Hz, the average RMS over 30-minute windows was calculated as 0.056 Pa using ObsPy (Beyreuther et al., 2010). Accounting for a 38 dB difference in transmission loss, we estimate an RMS pressure amplitude between 1.5–4.4 Pa. The measured RMS amplitude for the TA signal at TGY was calculated as 2.075 x 10^{-6} m/s. Following Anthony et al. (2022), the depth of sensitivity of the ground to the acoustic signal was calculated as 0.51 km based on 0.1 Hz frequency (supplemental Seismo-Acoustic Coupling Calculations section). This finding was combined with the CRUST1.0 model (Laske et al., 2013) Lamé constants, λ and μ, to calculate a transfer coefficient. The location of the station TGY is approximately at the intersection of 4 grid cells of the CRUST1.0 model, so we used the average of the 4 cells. The average λ is 6.1225 GPa, and the average μ is 0.646 GPa. This result gives a transfer coefficient of 5.263 x 10^{-7} m/s/Pa. Using this value and the RMS from the seismic station, the expected amplitude of the acoustic signal that could generate the seismic displacement is 3.94 Pa, which is within the expected range based on the RMS at recorded at I39PW. These findings confirm that it is reasonable for the TA seismic signal to originate from ground-coupled airwaves.

The TA signal also provides an empirical estimate of the travel time from Taal to I39PW (Figure 8). By cross-correlating the envelope of the low-frequency signal measured at TGY and I39PW, we can confirm the celerity range around 260 m/s that is simulated using ray theory (see section Infrasound Propagation Modeling). The uncertainty in the estimated travel time amounts to approximately 100 seconds.

Reduced displacement (Dr) is a distance-normalized measure of volcanic tremor amplitude that allows for comparison between eruptions (Aki and Koyanagi, 1981; McNut et al., 2015). Reduced displacement was calculated following the method of McNutt et al. (2015) for station TGY (Figure 9). Based on the bulk erupted volume of 0.04–0.1 km^3 from Balangue-Tarriela et al. (2022), the eruption had a Volcanic Explosivity Index (VEI) of 3 (Newhall and Self, 1982). Using the relationship between Dr and VEI, the expected Dr would be around 29 cm^2. However, the mean value of 351 cm^2 for this event corresponds to a VEI 5 according to the relationship presented in McNutt et al., (2015). This reduced displacement value is much larger than the January 1976 eruption of Augustine volcano (Dr 140 cm^2, VEI 4) and 18 May 1980 eruption of Mount St. Helens (Dr 260 cm^2, VEI 5) (McNutt, 1994). As noted by McNutt et al. (2015), tremor from fissures and phreatic eruptions tend to be stronger than other eruptions. This is consistent with reports of fissures (Philippine Institute of Volcanology and Seismology (PHIVOLCS-DOST) [PHIVOLCS], 2020), a dike intrusion (Bato et al., 2021), and the phreatomagmatic nature of the eruption. The implication is that the water-rich explosive eruption at Taal may have produced greater seismic tremor than would be expected from an eruption its size based on the tephra volume alone. However, this analysis is based on a single seismic station and there could be an impact on the estimate from path and site effects.

Combined Timeline and Plume Interpretation

Our interpretation of the multi-parameter dataset provides additional detail about the changing eruption dynamics through time. Figure 12 shows an overview of the eruptive sequence on 12 January, divided into five phases. In summary, Phase 1 is characterized by a low-level plume resulting from phreatic activity on the lake shore of the MCL, as reported by PHIVOLCS, which quickly transitioned into phreatomagmatic activity. Phase 2 produced an energetic, high-altitude plume detected by satellite, infrasound, and abundant lightning. Phase 3 created a less energetic but a still high-level plume (Figure 3), characterized by pulsatory activity in satellite imagery. The TA seismo-acoustic tremor signal was not present in this phase or any subsequent phases. In Phase 3 there was less energetic infrasound overall which was only recorded at station I39PW. Phase 4 marked a decrease in eruption intensity in all monitoring data available, and a transition to lower plumes with incandescence observed by PHIVOLCS and local eyewitnesses. Finally, Phase 5 marks the transition to low-level activity (plume heights <2 km) that continued until 22 January, with the PHIVOLCS alert level being lowered on 26 January. The following section provides a more detailed examination of each eruption phase.

Phase 1: Initiation of activity (12 January 2020 from 05:00 – 06:40 UTC)

The eruption on 12 January began on the northeast shore of the Main Crater Lake (MCL). Felt earthquake activity began around 03:00 UTC. Initially the eruption was characterized by low-level activity with small phreatic eruptions beginning at around 05:00 UTC as seen in the PHIVOLCS webcam (PHIVOLCS-DOST [@phivolcs_dost], 2020b) and video posted online (Figure 12, Adrian [SaiAdrian], 2020), defining the start of this eruption phase. Prior to this escalation, eyewitnesses also reported seeing a crack or fissure form within the crater. The location of this initial low-level activity was close to the shores of the lake and is characterized by what appears to be predominantly gas emissions in one of the fumarolic areas that quickly escalated. The source of emission appeared to migrate or expand into the lake before the webcam view was lost at around 06:15 (Table S3). Based on the webcam images from PHIVOLCS the eruption appeared to transitioned to phreatomagmatic toward the end of this phase, based on the increasing appearance of dark-colored plumes, suggesting involvement of fragmented magmatic particles (Table S3). During this initial activity there was no regional infrasound detected, no plume visible in Himawari-8 satellite, and no lightning detected by the GLD360 network.

Phase 2: High-level, sustained plume (12 January 2020 from 06:40 – 12:00 UTC)

The start of Phase 2 is defined by the initial arrival of infrasound to station I39PW (06:40) and growth of a plume detectable in Himawari-8 satellite images (by 06:33). This phase lasted from 06:40–12:00 and featured an eruptive plume with a sustained height from 16–17 km a.s.l. and maximum overshoot of 17.5 km. The height of the tropopause was 16.9 km based on the atmospheric sounding at 12:00 on 12 January 2020 from Mactan, Philippines, 500 km south of Taal (Van Eaton et al., 2022). Within this main phase we define two sub-phases, 2a and 2b.

Phase 2a from 06:40–08:20 is defined by the start of detectable infrasound, the TA signal, and volcanic lightning. The lightning increased to a steady flash rate, followed by a brief decrease before increasing into phase 2b. Plume height increased to a sustained altitude of around 16 km during this phase. The infrasound has a peak frequency of ~0.09 Hz and shows increasing acoustic power to its peak. Volcanic lightning was not detected by the GLD360 network until 07:03, indicating that the plume was not yet producing detectable (long-range) lightning even though infrasound signals were measured at station I39PW beginning at 06:45. Plume heights rose from 5–16 km in this time frame. Based on the plume height, infrasound acoustic power, and lightning increase, the eruption reached a sustained, high-level of intensity (Phase 2b) by 08:20.

Phase 2b (08:20 to ~12:00) is characterized by decreasing, but still elevated, acoustic power of the infrasound signal. Detections are present at all detecting remote infrasound stations in this time frame. The TA tremor signal at station TGY occurs by 07:00 (denoted by purple solid line in Figure 12) and ends by 12:00. There was a sustained, high-altitude volcanic plume up to the tropopause (between 16-17 km) as observed by Himawari-8 satellite. From 8:20 to 10:45 the infrasound peak frequency remains around 0.09 Hz (Figure S11) and the lightning flash rate increases to an average of 26 flashes min^{-1}. From about 10:45 to 12:00 the infrasound peak frequency and lightning flash rate steadily increase and the infrasound spectra narrow as lower frequency signals wane. In general, lower frequencies tend to have more acoustic power, so the decrease in acoustic power with increasing peak frequency is expected. The infrasound peak frequency stabilized around 0.2 Hz, about a factor of 2 increase, and the lightning flash rate peaked at 85 flashes per minute at 11:46.

Overall, all of phase 2 of the eruption is characterized by strong, band-limited (0.03–0.2 Hz) infrasound widely in the remote network, a high-level plume leveling off at around 16-17 km, lightning rates averaging 26 flashes min^{-1}, TA infrasound tremor signal at seismic station TGY, and photos and videos of a sustained, light-colored eruption column that appears to encompass the entire MCL area. The color of the column suggests a significant amount of water vapor and condensed droplets within the plume (Table S3). This interpretaion is supported by observations of wet ash and accretionary lapilli in the ashfall deposits (Balangue-Tarriela et al., 2022), and eyewitness reports of wet clumps of ash and/or mud falling. This phase lasts until around 12:00, during which the low-frequency infrasound signal is detected at IMS stations at longer ranges (e.g., up to 5,000 km). After this time only station I39PW detects infrasound from Taal.

The volcanic plume dynamics during Phase 2 are of particular interest because they represent the peak intensity of the eruption. There is an intriguing shift to higher peak frequency infrasound and a waning of lower frequency signals after ~10:45 (Figures 6, 8, S11), coincident with increasing lightning rates. Lightning production ramps up from 10:30–12:00 (Figures 4 and 12), yet the maximum plume heights remain stable at 16–17 km across this transition. The end of Phase 2 is defined by the end of the seismo-acoustic TA tremor signal, which may indicate a significant shift in eruption dynamics, as discussed below.

The increase in peak frequency observed after ~10:45 could originate from several changes, such as: (1) an increase in jet velocity; (2) decrease in jet diameter; or (3) change in the properties of the jet flow, for example, plume water content, grain size of particles, or a transition from a gas-rich to ash-rich plume, or a combination thereof. One possible explanation for the waning of low-frequency infrasound (increase in peak frequency) is that vaporization of water in the crater lake reduced the availability of external water, changing the dynamics of magma-water interaction.

We do not have direct evidence for when, exactly, the lake water disappeared. However, photographs and videos taken before, during, and after the eruption show that the plume originated under the lake and the water was gone by 02:33 on 13 January (Table S3). The simplest explanation is that the eruption vaporized the water and entrained it into the volcanic plume. Earlier in the 12 January eruption, before 10:45, the predominantly lower frequency infrasound (~0.09 Hz) may be explained by the eruption interacting with abundant lake water and creating a lower frequency source of resonance (cf. Fee et al., 2019). Similar changes were observed during the eruptions of Bogoslof, Alaska, in 2016–2017 and Anak Karakatau, Indonesia, in 2018, when the vent sites transitioned from subaqueous to subaerial (Fee et al., 2019; Perttu et al., 2020a). In both cases, the 'dry' plume produced higher frequency infrasound, and a significantly lower frequency infrasound signal emerged when the vent was inundated with water. The presence of low frequency infrasound in itself does not necessarily imply the interaction of water, but the shift through time, combined with other observations of the eruption behavior, help to put these signals into context.

When Taal's infrasound signal shifts to a higher peak frequency after 10:45, it is plausible that dwindling water levels began to change the dynamics of the eruption. A decrease in the jet diameter could produce higher frequency infrasound, but that would not explain the increase in lightning production observed at this time (Figure 12). Another possibility is that dwindling water levels led to a magma-water ratio enabling more efficient phreatomagmatic fragmentation (Wohletz, 1986). When there are large amounts of water relative to magma, incomplete water vaporization leads to a cooler, denser plume that entrains some liquid water droplets (rather than just water vapor) and makes the volcanic plume more likely to collapse (Koyaguchi and Woods, 1996). If lower water levels in the crater lake improved the efficiency of magma-water interaction, we might expect to see finer grained ash in the plume, which is linked to enhanced lightning production (Springsklee et al., 2022). However, it is also possible that this process could boost the overall plume heights (which was not observed), so no single explanation is entirely satisfactory. The observation that Taal's maximum plume heights topped out near the tropopause suggests that the plume rose convectively through the tropical atmosphere and may have been relatively insensitive to minor variations at the eruptive source (cf. Tupper et al. 2009). A detailed geologic study of the fall deposits from before and after 10:45 UTC would be needed to further investigate the possibility of a progressive decrease in the supply of water to erupting magma.

We also note that photographs and videos taken before, during, and after this key shift at ~10:45 do not show any obvious changes in the color of the main plume that might be attributed to major changes in water content. However, a secondary, much smaller plume (<2.5 km high) is also observed in several photographs and time-lapse images from 09:00 onward (Table S3), illustrating the complexity of the source and the potential for multiple vents.

Phase 3: Pulsatory eruptive activity (12 January 2020 from 12:00 - 17:30 UTC)

Phase 3 from 12:00–17:30 is characterized by unsteady, pulsating behavior of the plume. In the beginning of this phase we see a weakening of the plume, observed as a decrease in the upwind propagation of the umbrella. The first observable "pulse" occurred at 12:43, continuing until the high-level plume appears to detach from the vent at 17:33. During this phase there is also a slight shift in the peak frequency of infrasound at station I39PW and in the high frequency array processing results (Figure 6). As noted in the previous section, a change in frequency content that is remotely observed can be due to changes in the source as well as in the infrasonic propagation conditions along the propagation path. However, the stable propagation conditions throughout the day (Figures S12–S14) point to a change in the character of the eruption. The lightning flash rates peak just before 12:00 and then become more variable, correlating with the time frame of observed pulses within the plume (Figure 12). Lightning rates fall below 3 flashes min–1 at around 17:30.

Phase 4: Winding Down (12 January 2020 from 17:30–21:00)

Phase 4 from 17:30–21:00 is characterized by the winding down of explosive intensity. PHIVOLCS reported that beginning at 18:49 through 20:28 (after nightfall) there was incandescence observed in the plume, which may have indicated lava fountaining occurring after a shift from a phreatomagmatic to a magmatic behavior. This incandescence was documented by local photographers who reported that the glow was visible to the naked eye (Table S3; PHIVOLCS-DOST [@phivolcs_dost], 2020c; Quiambao, P., personal communication 27 August 2022; GMA News, 2020). However, it is unclear whether the incandescence merely became more visible during nighttime. This possible shift to fountaining and more magmatic eruption behavior is consistent with the vent becoming isolated from the lake due to vaporization, displacement of the water, or buildup of a cone around the vent that isolated it from the lake. However, in later photographs of the MCL area (Table S3 and Philippine Institute of Volcanology and Seismology (PHIVOLCS-DOST) [PHIVOLCS], 2020) show no evidence of a cone or spatter ramparts. It is our interpretation that the energetic infrasound, seismic, and lightning data, as well as the sustained high-altitude plume that was very light in color, indicate that most of the MCL water was vaporized and entrained into the plume during Phases 2–3. The shift to higher frequency infrasound signals at 13:12 (within Phase 3) may suggest when the vent began to dry out. The plume heights continue to wane and eventually become undetectable ~17:30 in the Himawari-8 satellite images, which corresponding to a change in lightning activity at 17:36. At this point, the eruption transitioned from a phreatomagmatic to magmatic eruption characterized by lava fountaining and low-level plumes. The initial phase of this transition was still detectable but soon fell below the detection limits for the remote data. Eruption intensity declined leading to the end of high intensity explosive activity around 21:00. Infrasound detections in both PMCC and the Fisher detector are greatly reduced at 14:15 and cease by around 20:00. The lightning flash rate falls below 3 per minute around 17:30 and finally ends after 18:13. Although there are no direct observations of the MCL available on 12 January, a Sentinel-2 scene acquired at 02:33 on 13 January shows a mostly dry, incandescent lakebed (Figure S3).

Phase 5: Continuation of low-level activity (through 26 January 2020 at 00:00)

Low-level activity characterized by the emission of small plumes < 2 km continued for several days. We end this phase with the lowering of the local alert level from level 4 to level 3 at 00:00 UTC on 26 January 2020. This phase of the eruption is not examined in any detail in our study, but it is worth noting there are several photos within this time frame showing a clear view of the MCL floor almost entirely devoid of standing water on both 16 and 21 January (Carn [@simoncarn], 2020; Tima [@raffytima], 2020; Table S3). In Bato et al. (2021), the emplacement of a dike was imaged in inSAR scenes from 9–17 January 2020, which they call the co-eruptive phase. Deformation within the dike was still observed during the post-eruptive phase extending to 4 February 2020, although it was limited to dike opening rather than propagation. This dike was modeled to extend from below the TVI through the MCL and out to the LT at a depth of <10 km.

Where did the Main Crater Lake water go?

The absence of the Main Crater Lake as evidenced through numerous photographs and satellite scenes in the days following the eruption presents an interesting puzzle. The pre-eruptive volume of the lake was calculated to be 42 million m^3 (Bernard et al., 2020), and in the two days before the eruption the temperature was measured at 31.1°C (PHIVOLCS, 2020p). The presence of the incandescence in Phase 4 leads to the interpretation that much of the water must have been previously removed in order for the vent to have been mostly dry. This is also supported by the lack of an obvious cone or similar structure that could have isolated the vent from the lake. This observation indicates that the majority of the lake water was removed within just under 12 hours.

Given the volume, and change in initial temperature from ~31° C, the amount of energy required to vaporize the entire lake was 1.07×10^{17} J. If most of the lake was vaporized in just under 12 hours, as we suggest, that would require 2.50×10^{12} W. Alternatively, if the Sentinel-2 overpass at 02:33 (Figure S3) is used as the 'end' of the lake water, then the vaporization would have required 1.42×10^{12} W (see supplementary Energy Calculation section). Given the volume of tephra calculated from the deposits reported in Balangue-Tarriela et al. (2022), which ranged from 0.04 km^3 to 0.1 km^3, and using average values for andesite specific heat capacity from Heap et al. (2020), of 0.7519 kJ·/kgK, there would need to be a 980°C decrease in magmatic temperatures to transfer enough energy to the water. These values represent an upper limit for several reasons. As noted by Bernard et al. (2020) there was an increase in CO_2 prior to the eruption, and the presence of excess dissolved CO_2 in the MCL could have decreased its boiling point. This would reduce the heat input required to boil off the lake. Additionally, it is likely that the water took other routes not limited to boiling off. Evidence from wet ashfall (Martinez-Villegas et al., 2022), accretionary lapilli, and light-colored plume support the idea that much of the water was incorporated into the wet plume, but some water may have escaped via alternative means (e.g., seepage), which has been known to occur at Taal (Bayani Cardenas et al., 2012). Water may have been incorporated into the plume as liquid droplets as well as vapor, entered cracks and pore space in the island, or been ejected out of the lake by explosions. Overpasses by the Korean satellite KOMPSAT-3A on 16 and 26 January 2020 showed the area of the crater on TVI beginning to refill with water, which illustrates the complex hydrologic system on the island (Del Castillo, 2020).

Conclusions

Our multi-parametric analysis from remote observations has identified five eruptive phases within the 12 January 2020 eruption of Taal Volcano. Specifically, our analysis illustrates a transition from the high-level, sustained ash emissions, to less energetic eruption by 12:00 UTC, and a shift to unsteady, pulsating activity in the plume. The sustained, high-level plume lasted around 4 hours as observed from remote infrasound data, the seismo-acoustic tremor TA signal and the high rate of volcanic lightning flashes. These findings add detail to the official reports available at the time of the eruption, which noted two main eruptive phases.

Our analysis suggests that the Main Crater Lake (MCL) was mostly vaporized and consumed by the eruption within Phases 1 and 2 corresponding with the TA seismic tremor signal and infrasound signal recorded at I39PW and totally dry by the end of Phase 3. The end of the high-intensity explosive activity on 12 January in Phase 4 appears to have been a ‘dry’ magmatic eruption which deposited material blanketing the earlier phreatomagmatic deposits on Taal Volcano Island (TVI). Future work on deposits (or erosive features) on the island could constrain the nature and timing of this intriguing transition. This was followed by a magmatic eruption characterized by incandescence or lava fountaining and low-level plume. While there was still some water involved, as is evident by the plume color on the 13 January, most of the water was already consumed or pushed out, either through cracks, incorporated in the plume, and/or through physical expulsion by this point.

During this eruption, local stations were destroyed, covered in ash, and/or impacted by power outages, disrupting the transmission of data. This issue is common in large, explosive eruptions, highlighting the value of remote and regional data for monitoring ongoing activity. While lower-level activity may only be recorded on local monitoring equipment, the higher-intensity (and potentially hazardous) phases of eruptions can be monitored with remote methods when local infrastructure is disrupted.

We envision an opportunity whereby local monitoring infrastructure could be supported by remote methods for data continuity and adding layers of observational detail. Recent studies have proposed an international remote sensing strategy for this purpose (Pritchard et al., 2022). In eruptions that produce volcanic lightning, global lightning detection networks provide robust datasets with high temporal resolution and are especially powerful when combined with other remote methods like infrasound, seismic, and satellite.

Data and Resources

Infrasound and seismic IMS data are available for researchers through the vDEC program with the CTBTO. The Singapore infrasound station SING is available upon request. Lightning data were provided by Vaisala Inc. Himawari-8 data were acquired from JMA. PlanetLabs data are accessed through the 'E&R The Smithsonian Institute PL-0036349' plan. Other satellite data are open access. Photographs were acquired from social media and traditional media sites that are publicly available. Software used included PMCC (available through CEA), ObsPy (Beyreuther et al., 2010), CRUST1.0 (Laske et al., 2013), Fisher beamforming (https://github.com/jdassink/beamforming; pysabeam (unreleased)) ,ePape (https://github.com/chetzer-ncpa/ncpaprop-release; Waxler et al., 2021; 2022), InfraGA (https://github.com/LANL-Seismoacoustics/infraGA; Blom, 2019).

Supplemental information file contains a table of abbreviations and variables used, a table of the PHIVOLCS and Tokyo VAAC alerts and bulletins, a table of the visual data used, a table of the infrasound stations and their distances and azimuths, as well as supplemental figures of further processing that was completed for this manuscript.

Acknowledgments

We would like to first of all thank PHIVOLCS for excellent documentation during the eruption crisis and for continued discussions throughout this project. We would also like to thank Evie Snee for help with the initial project. We would like to thank Steven Gibbons for helpful discussions on slowness corrections for seismic arrays. We would like to thank David Green, and three anonymous reviewer for their comments which improved this manuscript.

SD was supported by the Royal Society grant IES\R2\202007. This research was supported in part by the Earth Observatory of Singapore via its funding from the National Research Foundation Singapore and the Singapore Ministry of Education under the Research Centres of Excellence initiative. This work comprises EOS contribution number 489. The authors thank the CTBTO and station operators for the high quality of IMS data and products. IMS data can be accessed through the vDEC (see https://www.ctbto.org/specials/vdec/). AP, BP and GL are supported through funding from the Volcano programme of the ‘Resilience to Nature’s Challenges’ National Science Challenge of New Zealand (GNS-RNC047). Any use of trade, firm, or product names is for descriptive purposes only and does not imply endorsement by the U.S. Government.

Declaration of Competing Interests

The authors acknowledge there are no conflicts of interest recorded.

References

Abanto, R. (2023). Some families still awaiting relocation 3 years after Taal eruption: <https://news.abs-cbn.com/video/spotlight/01/12/23/some-families-still-awaiting-relocation-after-taal-2020-eruption> (accessed January 2023).

Aki, K., and R. Koyanagi (1981). Deep volcanic tremor and magma ascent mechanism under Kilauea, Hawaii, *J. Geophys. Res.-Sol. Ea.* 7095-7109. https://doi.org/10.1029/JB086iB08p07095

Adrian, S. [SaiAdrian] (2020). ACTUAL FOOTAGE OF TAAL VOLCANO STARTING TO EXPLODE 🌋 12:30pm January 12, 2020. https://youtu.be/8s_R3jRz32g

Anthony, R.E., A. T. Ringler, T. Tanimoto, R. S. Matoza, S. De Angelis, and D. C. Wilson (2022). Earth’s Upper Crust Seismically Excited by Infrasound from the 2022 Hunga Tonga-Hunga Ha’apai Eruption, Tonga, *Seismol. Res. Lett.* 1-4. https://doi.org/10.1785/0220220252

Assink, J. D., R. Waxler, and D. Drob (2012). On the sensitivity of infrasonic traveltimes in the equatorial region to the atmospheric tides, *J. Geophys. Res. Atmos*., 117, no. D1, https://doi.org/10.1029/2011JD016107

Assink, J., R. Waxler, and D. Velea (2017). A wide-angle high Mach number modal expansion for infrasound propagation, *J. Acoust. Soc. Am.*, 141, no. 3, 1781–1792, https://doi.org/10.1121/1.4977578

Assink, J., Smets, P., Marcillo, O., Weemstra, C., Lalande, J. M., Waxler, R., & Evers, L.

(2019). Advances in infrasonic remote sensing methods. In Infrasound monitoring for atmospheric studies (pp. 605-632). Springer, Cham.

Bachmeier, S. (2020). Eruption of the Taal Volcano in the Philippines, CIMSS Satellite Blog, <https://cimss.ssec.wisc.edu/satellite-blog/archives/35406> (accessed October 2022).

Balangue-Tarriela, M. I. R. et al. (2022). Analysis of the 2020 Taal Volcano tephra fall deposits from crowdsourced information and field data, *Bull. Volcanol*., 84, no. 3, 35, https://doi.org/10.1007/s00445-022-01534-y

Bato, M. G., P. Lundgren, V. Pinel, R. Solidum Jr., A. Daag, and M. Cahulogan (2021). The 2020 Eruption and Large Lateral Dike Emplacement at Taal Volcano, Philippines: Insights From Satellite Radar Data, *Geophys. Res. Lett.*, 48, no. 7, e2021GL092803. https://doi.org/10.1029/2021GL092803

Bayani Cardenas, M., A. M. F. Lagmay, B. J. Andrews, R. S. Rodolfo, H. B. Cabria, P. B. Zamora, and M. R. Lapus (2012). Terrestrial smokers: Thermal springs due to hydrothermal convection of groundwater connected to surface water, *Geophys. Res. Lett.*, 39, no. 2. https://doi.org/10.1029/2011GL050475

Bernard, A., E. Villacorte, K. Maussen, C. Caudron, J. Robic, R. Maximo, R. Rebadulla, Ma. a. V. Bornas, and R. U. Solidum Jr. (2020). Carbon Dioxide in Taal Volcanic Lake: A Simple Gasometer for Volcano Monitoring, *Geophys. Res. Lett.*, 47, no. 24, e2020GL090884. https://doi.org/10.1029/2020GL090884

Beyreuther, M., R. Barsch, L. Krischer, T. Megies, Y. Behr and J. Wassermann (2010). ObsPy: A Python Toolbox for Seismology, *Seismol. Res. L*ett., 81(3), 530-533. https://doi.org/10.1785/gssrl.81.3.530

Bishop, J.W., D. Fee, R. Modrak, C. Tape, and K. Kim (2022). Spectral Element Modeling of Acoustic to Seismic Coupling over Topography (2022). *J. Geophys. Res. Solid Earth*, 127. https://doi.org/10.1029/2021JB023142

Blom, P. (2019). Modeling infrasonic propagation through a spherical atmospheric layer—Analysis of the stratospheric pair, *J. Acoust. Soc. Am.*, 145, no. 4, 2198–2208. https://doi.org/10.1121/1.5096855

Bryan, C. J., and S. Sherburn (1999). Seismicity associated with the 1995–1996 eruptions of Ruapehu volcano, New Zealand: narrative and insights into physical processes, *J. Volcanol. Geotherm. Res.*, 90, no. 1, 1–18. https://doi.org/10.1016/S0377-0273(99)00016-5.

Cansi, Y. (1995). An automatic seismic event processing for detection and location: The P.M.C.C. Method, *Geophys. Res. Lett.*, 22, no. 9, 1021–1024. https://doi.org/10.1029/95GL00468.

Carn, S. [@simoncarn] (2020). A @planetlabs image timelapse (Dec 24, 2019 - Jan 16, 2020) showing the dramatic changes in the main crater of #TaalVolcano after the Jan 12-13 #eruption. #TaalVolcanoEruption #TaalEruption2020 @phivolcs_dost @nababaha @EarthUncutTV @raffytima https://t.co/4JkgFgH7no, Tweet.

Caudron, C., B. Taisne, M. Garces, A. Le Pichon, P. Mialle (2015). On the use of remote infrasound and seismic stations to constrain the eruptive sequence and intensity for the 2014 Kelud eruption, *Geophys. Res. Lett.*, 42, no. 16, 6614-6621. https://doi.org/10.1002/2015GL064885.

Chen, J. (2020). Manila Airport partially reopens after Taal volcano eruption leads to over 240 cancelled flights: <https://www.businesstraveller.com/business-travel/2020/01/13/manila-airport-partially-reopens-after-taal-volcano-eruption-leads-to-over-240-cancelled-flights/> (accessed October 2022).

Coombs, M.L., A.G. Wech, M.M. Haney, J.J. Lyons, D.J. Schneider, H.F. Schwaiger, K.L. Wallace, D. Fee, J.T. Freymueller, J.R. Schaefer, and G. Tepp (2018). Short-term forecasting and detection of explosions during the 2016–2017 eruption of Bogoslof Volcano, Alaska, *Front. Earth Sci.*, 6, no. 122.https://doi.org/10.3389/feart.2018.00122

Del Castillo, F. P., P.M.J. Paraiso, M.C.T.M. Vicente, L.P. Jamero, G.T. Narisma (2020). Impacts of Taal Volcano Phreatic Eruption (12 January 2020) on the Environment and Population: Satellite-Based Observations Compared with Historical Records | Manila Observatory, <https://www.observatory.ph/2020/04/20/impacts-of-taal-volcano-phreatic-eruption-12-january-2020-on-the-environment-and-population-satellite-based-observations-compared-with-historical-records/> (accessed October 2022).

Delos Reyes, P. J., Ma. A. V. Bornas, D. Dominey-Howes, A. C. Pidlaoan, C. R. Magill, and Jr. Solidum Renato U. (2018). A synthesis and review of historical eruptions at Taal Volcano, Southern Luzon, Philippines, *Earth-Sci. Rev.*, 177, 565–588. https://doi.org/10.1016/j.earscirev.2017.11.014

den Ouden, O.F.C., J.D. Assink, P.S.M. Smets. S. Shani-Kadmiel, G. Averbuch, L.G. Evers (2020). CLEAN beamforming for the enhanced detection of multiple infrasonic sources, *Geophys. J. Int.*, 221, no. 1, 305-317. https://doi.org/10.1093/gji/ggaa010

DOST-PHIVOLCS (2021). 2020 Annual Report. <https://www.phivolcs.dost.gov.ph/index.php/publications/annual-report> (accessed October 2022).

Drob, D. (2019). Meteorology, Climatology, and Upper Atmospheric Composition for Infrasound Propagation Modeling, in: Infrasound Monitoring for Atmospheric Studies, 485–508.

Endo, E. T., T. Murray (1991). Real-time Seismic Amplitude Measurement (RSAM): a volcano monitoring and prediction tool, *Bull. Volcanol.*, 55, 533-545. https://doi.org/10.1007/BF00298154

Fee, D., J. Lyons, M. Haney, A. Wech, C. Waythomas, A. K. Diefenbach, T. Lopez, A. Van Eaton, and D. Schneider (2019). Seismo-acoustic evidence for vent drying during shallow submarine eruptions at Bogoslof volcano, Alaska, *Bull. Volcanol.*, 82, no. 1, 2. https://doi.org/10.1007/s00445-019-1326-5

Fee, D., and R. S. Matoza (2013). An overview of volcano infrasound: From Hawaiian to Plinian, local to global, *J. Volcanol. Geotherm. Res.*, 249, 123–139. https://doi.org/10.1016/j.jvolgeores.2012.09.002

Flanagan, M. P., S. C. Myers, and N. A. Simmons (2012). Model-based corrections to observed back azimuth and slowness observations from a dipping Mohorovicic discontinuity, LLNL-CONF-563592, Lawrence Livermore National Lab (LLNL), Livermore, CA (United States).

Global Volcanism Program (2020). Report on Taal (Philippines): <https://doi.org/10.5479/si.GVP.BGVN202006-273070> (accessed November 2022).

Heap, M. J., A. R. L. Kushnir, J. Vasseur, F. B. Wadsworth, P. Harlé, P. Baud, B. M.

Kennedy, V. R. Troll, and F. M. Deegan (2020). The thermal properties of porous andesite, *J. Volcanol. Geotherm. Res.*, 398, 106901. https://doi.org/10.1016/j.jvolgeores.2020.106901

Koyaguchi, T. and A.W. Woods (1996). On the formation of eruption columns following explosive mixing of magma and surface water, *J. Geophys. Res.*, 101, 5561-5574.

Laske, G., G. Masters, and M. Pasyanos (2013). Update on CRUST1.0 - A 1-degree Global Model of Earth's Crust, EGU2013-2658.

Martinez-Villegas, M. (2020). Volcano risk communication in the Philippines: Challenges, lessons and opportunities Taal volcano 2020. Retrieved from https://drive.google.com/file/d/1sUrKHfObZKDBA8y1sDlNr9_CcqPORSWB/view?usp=sharing

Martinez-Villegas, Ma. M., P. D. Reniva, L. R. D. Sanico, A. R. Loza, R. G. Seda, D. F. Doloiras, and A. C. Pidlaoan (2022). Perspectives on the 12 January 2020 Taal Volcano eruption: An analysis of residents' narrative accounts, *Front. Earth Sci.*, https://doi.org/10.3389/feart.2022.923224

Mastin, L. G., and A. R. Van Eaton (2020). Comparing Simulations of Umbrella-Cloud Growth and Ash Transport with Observations from Pinatubo, Kelud, and Calbuco Volcanoes, 10, *Atmos.*, 11, no. 10, 1038. https://doi.org/10.3390/atmos11101038

Matoza, R. S., M. Landès, A. Le Pichon, L. Ceranna, and D. Brown (2013). Coherent ambient infrasound recorded by the International Monitoring System, *Geophys. Res. Lett.*, 40, no. 2, 429–433. https://doi.org/10.1029/2012GL054329

Matoza, R. S., D. Fee, D. Green, and P. Mialle (2019). Volcano Infrasound and the International Monitoring System, In: Infrasound monitoring for atmospheric studies (pp. 1023-1077). Springer, Cham

Matoza, R. S., and D. C. Roman (2022). One hundred years of advances in volcano seismology and acoustics, *Bull. Volcanol.*, 84, no. 9, 86. https://doi.org/10.1007/s00445-022-01586-0

McKee, K., C. M. Smith, K. Reath, E. Snee, S. Maher, R. S. Matoza, S. Carn, L. Mastin, et al. (2021). Evaluating the state-of-the-art in remote volcanic eruption characterization Part I: Raikoke volcano, Kuril Islands, *J. Volcanol. Geotherm. Res.*, 419, 107354. https://doi.org/10.1016/j.jvolgeores.2021.107354

McKee, K., C. M. Smith, K. Reath, E. Snee, S. Maher, R. S. Matoza, S. Carn, D. C. Roman, et al. (2021). Evaluating the state-of-the-art in remote volcanic eruption characterization Part II: Ulawun volcano, Papua New Guinea, *J. Volcanol. Geotherm. Res.*, 420, 107381. https://doi.org/10.1016/j.jvolgeores.2021.107381

McNutt, S.R. (1994). Volcanic tremor amplitude correlated with eruption explosivity and its potential use in determining ash hazards to aviation. In: Proceedings of the First International Symposium on Volcanic Ash and Aviation Safety. *U.S. Geol. Surv. Bull.*, vol. 2047, pp. 377 e385

McNutt, S. R., G. Thompson, J. Johnson, S. D. Angelis, and D. Fee (2015). Seismic and Infrasonic Monitoring, in: The Encyclopedia of Volcanoes, Elsevier, 1071–1099

Melton, B. S., and L. F. Bailey (1957). Multiple signal correlators, Geophysics, 22, no. 3, 565–588. https://doi.org/10.1190/1.1438390

Newhall, C. G., and S. Self (1982). The volcanic explosivity index (VEI): An estimate of explosive magnitude for historical volcanism. *J. Geophys. Res.*, 87(C2), 1231–1238. https://doi.org/10.1029/JC087iC02p01231

Oppenheimer, C. (1998). Review article: Volcanological applications of meteorological satellites, *Int. J. Remote Sens.*, 19, no. 15, 2829–2864. https://doi.org/10.1080/014311698214307

Perttu, A., C. Caudron, J.D. Assink, D. Metz, D. Tailpied, B. Perttu, C. Hibert, D. Nurfiani, C. Pilger, M. Muzli, D. Fee, O.L. Andersen, B. Taisne (2020a). Reconstruction of the 2018 tsunamigenic flank collapse and eruptive activity at Anak Krakatau based on eyewitness reports, seismo-acoustic and satellite observations, *Earth Planet. Sci. Lett.*, 541, 116268. https://doi.org/10.1016/j.epsl.2020.116268

Perttu, A., B. Taisne, S. De Angelis, J. D. Assink, D. Tailpied, and R. A. Williams (2020b). Estimates of plume height from infrasound for regional volcano monitoring, *J. Volcanol. Geotherm. Res.*, 402, 106997. https://doi.org/10.1016/j.jvolgeores.2020.106997

Philippine Institute of Volcanology and Seismology (PHIVOLCS-DOST) [PHIVOLCS] (2020). LOOK: The #TaalVolcano Main Crater after the 12 January 2020 eruption. The crater floor is now occupied by newly erupted ash. Several eruption vents where active steaming occurs have formed. The Main Crater Lake Islet (Vulcan Point) survived the eruption. On-going eruption activity may further change this crater morphology. #ScienceForThePeople #TaalEruption2020 (Interpreted on 24 January 2020) | Facebook: <https://www.facebook.com/PHIVOLCS/photos/a.285127764929462/2537055609736655/> (accessed October 2022).

Philippine Statistics Authority (2021). 2020 Census of Population and Housing Results (City of Manila) | Philippine Statistics Authority National Capital Region: <http://rssoncr.psa.gov.ph/article/2020-census-population-and-housing-results-city-manila> (accessed October 2022).

PHIVOLCS (2020a). Taal volcano bulletin update 12 January 2020 04:00 P.M: <https://www.phivolcs.dost.gov.ph/index.php/volcano-hazard/volcano-bulletin2/taal-volcano/9619-taal-volcano-bulletin-update-12-january-2020-04-00-pm-2> (accessed October 2022)

PHIVOLCS (2020b). Taal Volcano Bulletin 12 January 2020 02:30 P.M.: <https://www.phivolcs.dost.gov.ph/index.php/volcano-hazard/volcano-bulletin2/taal-volcano/9617-taal-volcano-bulletin-12-january-2020-02-30-pm> (accessed October 2022)

PHIVOLCS (2020c). Taal volcano bulletin 12 January 2020 07:30 P.M.: <https://www.phivolcs.dost.gov.ph/index.php/volcano-hazard/volcano-bulletin2/taal-volcano/9620-taal-volcano-bulletin-12-january-2020-07-30-pm>

PHIVOLCS (2020d). Taal volcano bulletin 13 January 2020 8:00 A.M.: <https://www.phivolcs.dost.gov.ph/index.php/volcano-hazard/volcano-bulletin2/taal-volcano/9625-taal-volcano-bulletin-13-january-2020-8-00-a-m>

PHIVOLCS (2020e). Eruption update for Taal volcano 13 January 2020 04:00 P.M.: <https://www.phivolcs.dost.gov.ph/index.php/volcano-hazard/volcano-bulletin2/taal-volcano/9633-eruption-update-for-taal-volcano-13-january-2020-04-00-pm>

PHIVOLCS (2020f). Taal volcano bulletin 14 January 2020 8:00 A.M.: <https://www.phivolcs.dost.gov.ph/index.php/volcano-hazard/volcano-bulletin2/taal-volcano/9636-taal-volcano-bulletin-14-january-2020-8-00-a-m>

PHIVOLCS (2020g). Taal volcano bulletin 15 January 2020 8:00 A.M.: <https://www.phivolcs.dost.gov.ph/index.php/volcano-hazard/volcano-bulletin2/taal-volcano/9642-taal-volcano-bulletin-15-january-2020-8-00-a-m>

PHIVOLCS (2020h). Taal volcano bulletin 16 January 2020 8:00 A.M.: <https://www.phivolcs.dost.gov.ph/index.php/volcano-hazard/volcano-bulletin2/taal-volcano/9647-taal-volcano-bulletin-16-january-2020-8-00-a-m>

PHIVOLCS (2020i). Taal volcano bulletin 17 January 2020 8:00 A.M.: <https://www.phivolcs.dost.gov.ph/index.php/volcano-hazard/volcano-bulletin2/taal-volcano/9653-taal-volcano-bulletin-17-january-2020-8-00-a-m>

PHIVOLCS (2020j). Taal volcano bulletin 18 January 2020 8:00 A.M.: <https://www.phivolcs.dost.gov.ph/index.php/volcano-hazard/volcano-bulletin2/taal-volcano/9659-taal-volcano-bulletin-18-january-2020-8-00-a-m>

PHIVOLCS (2020k). Taal volcano bulletin 19 January 2020 8:00 A.M.: <https://www.phivolcs.dost.gov.ph/index.php/volcano-hazard/volcano-bulletin2/taal-volcano/9665-taal-volcano-bulletin-19-january-2020-8-00-a-m>

PHIVOLCS (2020l). Taal volcano bulletin 20 January 2020 8:00 A.M.: <https://www.phivolcs.dost.gov.ph/index.php/volcano-hazard/volcano-bulletin2/taal-volcano/9671-taal-volcano-bulletin-20-january-2020-8-00-a-m>

PHIVOLCS (2020m). Taal volcano bulletin 21 January 2020 8:00 A.M.: <https://www.phivolcs.dost.gov.ph/index.php/volcano-hazard/volcano-bulletin2/taal-volcano/9675-taal-volcano-bulletin-21-january-2020-8-00-a-m>

PHIVOLCS (2020n). Taal volcano advisory 22 January 2020 04:00 P.M.: <https://www.phivolcs.dost.gov.ph/index.php/volcano-hazard/volcano-bulletin2/taal-volcano/9679-taal-volcano-advisory-22-january-2020-04-00-pm>

PHIVOLCS (2020o). General Location of Fissures Related to the January 2020 Taal Volcano Eruptive Activity.: <https://www.phivolcs.dost.gov.ph/index.php/news/9662-general-location-of-fissures-related-to-the-january-2020-taal-volcano-eruptive-activity>

PHIVOLCS (2020p). Taal volcano bulletin 10 January 2020 8:00 A.M.: <https://www.phivolcs.dost.gov.ph/index.php/volcano-hazard/volcano-bulletin2/taal-volcano/9605-taal-volcano-bulletin-10-january-2020-8-00-a-m>

PHIVOLCS-DOST [@phivolcs_dost] (2020a). Ongoing phreatic explosion at the Main Crater of Taal Volcano. Photos taken from installed IP camera monitoring the activity of Taal Volcano. https://t.co/9Qyd7aLvsJ, Tweet.

PHIVOLCS-DOST [@phivolcs_dost] (2020b). Inside the Taal Volcano Main Crater taken on January 12, 2020. The eruption was captured by PHIVOLCS IP camera at 5-minute interval from 1 PM to 3 PM. #HandaAngMayAlam #TaalVolcano #TaalEruption2020 https://t.co/kA2HZ4aYQs, Tweet.

PHIVOLCS-DOST [@phivolcs_dost] (2020c). Lava fountain from Taal Volcano Main Crater @3:20AM https://t.co/YmLaMJU1vQ, Tweet.

Poland, M.P., T. Lopez, R. Wright, and M.J. Pavolonis (2020). Forecasting, Detecting, and Tracking Volcanic Eruptions from Space, *Remote Sens. Earth Syst. Sci.*, 3, no. 1-2, 55-94. https://doi.org/10.1007/s41976-020-00034-x

Pritchard, M. E., M. Poland, K. Reath, B. Andrews, M. Bagnardi, J. Biggs, S. Carn, D. Coppola, S. K. Ebmeier, M. A. Furtney, T. Girona, J. Griswold, T. Lopez, P. Lundgren, S. Ogburn, M. Pavolonis, E. Rumpf, G. Vaughan, C. Wauthier, R. Wessels, R. Wright, K. R. Anderson, M. G. Bato, and A. Roman (2022). Optimizing Satellite Resources for the Global Assessment and Mitigation of Volcanic Hazards—Suggestions from the USGS Powell Center Volcano Remote Sensing Working Group. Scientific Investigations Report 2022-5116. https://doi.org/10.3133/sir20225116

Reuters (2020). Philippines suspends Manila airport flights as volcano spews ash | Reuters: <https://www.reuters.com/article/us-philippines-volcano-taal-airport-idUSKBN1ZB0A9> (accessed October 2022).

Sabillo, K. (2020). Phivolcs cleans up ash-covered instruments, sets up new stations near Taal Volcano | ABS-CBN News: <https://news.abs-cbn.com/news/01/15/20/phivolcs-cleans-up-ash-covered-instruments-sets-up-new-stations-near-taal-volcano> (accessed October 2022).

Sabillo [@kristinesabillo] (2020). LOOK: Phivolcs monitoring station in Agoncillo, Batangas. The solar panel is completely covered in ash, making it impossible for the station to transmit its data. Phivolcs has deployed teams to clean and check on its stations around Taal. Photo from Phivolcs. @ABSCBNNews https://t.co/GBH8Xt163z, Tweet.

Said, R. K., U. S. Inan, and K. L. Cummins (2010). Long-range lightning geolocation using a VLF radio atmospheric waveform bank, *J. Geophys. Res. Atmos.*, 115, no. D23. https://doi.org/10.1029/2010JD013863

Santos, J., K. I. D. Z. Roquel, A. Lamberte, R. R. Tan, K. B. Aviso, J. F. D. Tapia, C. A. Solis, and K. D. S. Yu (2022). Assessing the economic ripple effects of critical infrastructure failures using the dynamic inoperability input-output model: a case study of the Taal Volcano eruption, *Sustain. Resilient Infrastruct.*, 1–17. https://doi.org/10.1080/23789689.2022.2127999

Smart, E., and E. A. Flinn (1971). Fast Frequency-Wavenumber Analysis and Fisher Signal Detection in Real-Time Infrasonic Array Data Processing, *Geophys. J. Int.*, 26, nos. 1–4, 279–284. https://doi.org/10.1111/j.1365-246X.1971.tb03401.x

Smets, P. S. M., J. D. Assink, A. Le Pichon, and L. G. Evers (2016). ECMWF SSW forecast evaluation using infrasound, *J. Geophys. Res. Atmos.*, 121, no. 9, 4637–4650. https://doi.org/10.1002/2015JD024251

Smink, M. M., Assink, J. D., Bosveld, F. C., Smets, P. S., & Evers, L. G. (2019). A Three-Dimensional Array for the Study of Infrasound Propagation Through the Atmospheric Boundary Layer. *J. Geophys. Res. Atmos.*, 124(16), 9299-9313.

Spingsklee, C., B. Scheu, M. Manga, V. Cigala, C. Cimarelli, D.B. Dingwell (2022). The Influence of Grain Size Distribution on Laboratory-Generated Volcanic Lightning, *J. Geophys. Res. Solid Earth*, 127, no. 10. https://doi.org/10.1029/2022JB024390

Sutherland, L. C., and H. E. Bass (2004). Atmospheric absorption in the atmosphere up to 160 km, *J. Acoust. Soc. Am.*, 115, no. 3, 1012–1032. https://doi.org/10.1121/1.1631937

Thouret, J.-C., K. E. Abdurachman, J.-L. Bourdier, and S. Bronto (1998). Origin, characteristics, and behaviour of lahars following the 1990 eruption of Kelud volcano, eastern Java (Indonesia), *Bull. Volcanol.*, 59, no. 7, 460–480. https://doi.org/10.1007/s004450050204

Tima [@raffytima] (2020). After the phreatic eruption last Sunday and its continuous volcanic activity, the picture perfect features of Taal Volcano has changed. Compared to the photo taken by @ruthcabal15 last December, the famed Taal volcanic lake has disappeared in the drone photo I took today. https://t.co/AVPzZvcjOa, Tweet.

Tokyo VAAC (2020). Tokyo VAAC | Volcanic Ash Advisories: <https://ds.data.jma.go.jp/svd/vaac/data/vaac_list.html> (accessed October 2022).

UB: Pagbuga ng lava ng Taal Volcano, maituturing na “low-level eruption” (2020). Youtube.< https://youtu.be/iM8zBe9mH8E> (accessed October 2022).

Tupper, A., C. Textor, M. Herzog, H.F. Graf, M.S. and Richards (2009). Tall clouds from small eruptions: the sensitivity of eruption height and fine ash content to tropospheric instability, *Nat. Hazards*, 51, no. 2, 375-401. https://doi.org/10.1007/s11069-009-9433-9

Utami, S. B., F. Costa, P. Lesage, P. Allard, and H. Humaida (2021). Fluid Fluxing and Accumulation Drive Decadal and Short-Lived Explosive Basaltic Andesite Eruptions Preceded by Limited Volcanic Unrest, *J. Petrol.*, 62, no. 11, egab086. https://doi.org/10.1093/petrology/egab086

Van Eaton, A.R., Á. Amigo, D. Bertin, L.G. Mastin, R.E. Giacosa, J. González, O. Valderrama, K. Fontijn, and S.A. Behnke (2016). Volcanic lightning and plume behavior reveal evolving hazards during the April 2015 eruption of Calbuco volcano, Chile, *Geophys. Res. Lett.*, 43, 3563–3571. https://doi.org/10.1002/2016GL068076

Van Eaton, A.R., D.J. Schneider, C.M. Smith, M.M. Haney, J.J. Lyons, R. Said, D. Fee, R.H. Holzworth, and L.G. Mastin (2020). Did ice-charging generate volcanic lightning during the 2016–2017 eruption of Bogoslof volcano, Alaska, *Bull. Volcanol.*, 80, no. 24. https://doi.org/10.1007/s00445-019-1350-5

Van Eaton, A. R., C. M. Smith, M. Pavolonis, and R. Said (2022). Eruption dynamics leading to a volcanic thunderstorm—The January 2020 eruption of Taal volcano, Philippines, *Geology*, 50, no. 4, 491–495. https://doi.org/10.1130/G49490.1

Waxler, R., C. Hetzer, J. Assink, and D. Velea (2021). chetzer-ncpa/ncpaprop-release:

NCPAprop v2.1.0 | Zenodo: <https://zenodo.org/record/5562713#.Y1Xw0HZByUk> (accessed October 2022).

Waxler, R., Hetzer, C. H., Assink, J. D., & Blom, P. (2022). A two-dimensional effective sound speed parabolic equation model for infrasound propagation with ground topography. *J. Acoust. Soc. Am*., 152(6), 3659-3669.

Waxler, R., and J. Assink (2019). Propagation modeling through realistic atmosphere and benchmarking. In: Infrasound monitoring for atmospheric studies (pp. 509-549). Springer, Cham.

Wohletz, K.H. (1986). Explosive magma-water interactions: Thermodynamics, explosion mechanisms, and field studies, *Bull. Volcanol.*, 48, 245-265

Zimanowski, B. (1998). Phreatomagmatic Explosions., in: From Magma to Tephra: Modelling Physical Processes of Explosive Volcanic Eruptions A. Freundt, and M. Rosi (Editors), Elsevier Science, Amsterdam.

Full mailing address for each author

Anna Perttu
Volcanic Risk Solutions
Massey University
Private Bag 11 222
Palmerston North
New Zealand, 4442
Jelle Assink,
R&D Department of Seismology and Acoustics
Royal Netherlands Meteorological Institute (KNMI)
Postbus 201, 3730 AE
De Bilt, Netherlands

Alexa R. Van Eaton,
U.S. Geological Survey,
Cascades Volcano Observatory,

1300 SE Cardinal Ct,
Vancouver, WA 98683, USA

Corentin Caudron,
Université Libre de Bruxelles,
Av. Franklin Roosevelt 50,
1050 Bruxelles, Belgium

Chris Vagasky,
Vaisala Inc,
194 Taylor Ave,
Louisville, CO 80027, USA

Janine Krippner,
University of Waikato
Private Bag 3105
Hamilton 3240
New Zealand

Kathleen McKee,
University of Maryland Baltimore County
1000 Hilltop Cir,
Baltimore, MD 21250, USA

Silvio De Angelis,
School of Environmental Sciences,
University of Liverpool,
Brownlow Hill,
Liverpool,
L69 7ZX
UK

Brian Perttu,
Volcanic Risk Solutions,
Massey University
Private Bag 11 222
Palmerston North
New Zealand, 4442

Benoit Taisne,
Earth Observatory of Singapore,
Nanyang Technological University,
50 Nanyang Ave
Singapore 639798

Gert Lube,
Volcanic Risk Solutions,
Massey University
Private Bag 11 222
Palmerston North
New Zealand, 4442

Tables

TABLE 1: Eigenray parameters for the rays from Taal to I39PW (see Figure 7).

ray	inclination (deg)	azimuth (deg)	bounces	travel time (s)	celerity (m/s)	turning height (km)	back azimuth (deg)	trace velocity (m/s)
1	14.8	115.4	3	6322	260	114.3	298.4	349

2	26.4	115.6	4	6773	242	117.5	298.5	375

List of Figure Captions

Figure 1: Regional map on the left, showing the remote network used in the study, and indicating infrasound arrays (circles), seismic arrays (stars), and distances from the volcano. On the right, volcano area map and annotated satellite images showing the Taal caldera, Volcano Island (TVI) in Taal Lake (TL), and features on the island, including the Main Crater Lake (MCL), and the initial eruption site. Modified from Global Volcanism Program, 2020. Imagery courtesy of Planet Inc.

Figure 2: Timeline of Taal Volcano's climactic eruption 12–13 January 2020 from Philippine Institute of Volcanology and Seismology (PHIVOLCS) bulletin reports (red triangles) and Tokyo Volcanic Ash Advisory Center (VAAC) alerts (blue circles). Open circles indicate when the plume was reported as detached from the vent. Possible influence of meteorologic cloud cover was noted after the blue dashed line. The PHIVOLCS alert level is plotted as a colored background with Alert level 1 in green, 2 in yellow, 3 in orange, and 4 in red. Time frame of lava fountaining reported by PHIVOLCS is noted. Local day and night are also highlighted.

Figure 3: Top figure showing there was limited coverage by satellites; open circles are passes that actually cover the area of interest (crater of Taal Volcano) but didn't image the eruption. The Himawari-8 satellite, a geostationary meteorological satellite with a 10 minute repeat, provided the most coverage. Bottom figure showing the Himawari-8 plume height retrievals (in black), with red open circles indicating where the plume may actually be higher. The dashed blue lines indicate times when a pulsating plume can be seen in the Himawari-8 images.

Figure 4: Rates of volcanic lightning produced by the Taal eruption plume as detected by the GLD360 network from Van Eaton et al. (2022). (A) rates of all lightning flashes

within 200 km of the vent; (B) rates of distal lightning, defined by flashes occurring 20–200 km from vent; and (C) local lightning within 20 km of vent. Orange symbols give the per-minute flash rates and black line shows the 5-minute running average. Volcanic lightning was first detected at 07:03:02 UTC on 12 January 2020. The dataset was then visually divided into several stages of electrical activity (A-E) based on changes in the flash rate.

Figure 5: Summary of Progressive Multi-Channel Correlation (PMCC) results highlighting infrasound detections of the Taal eruption in red along with the background array processing results for each infrasound array in the region. The standard IMS array processing configuration was used. Stations are plotted in green (detection) or red (no detection), with the rose diagram of detections for 12 and 13 January 2020. Station I40PG had data quality issues and while the eruption was detected, the station does not have reliable array processing results. Results are inferred to be related to volcanic activity based on back azimuth and timing of detections.

Figure 6: Analysis of infrasound signals from the I39PW array, focusing on the eruption of Taal Volcano on 12 January 2020. The results have been adjusted for a propagation time of 6322 seconds to relate infrasonic features to eruptive activity. The spectrograms (A, B) and best beam (C) have been computed using the slowness vector estimates obtained over the 0.07–1.0 Hz band. The dashed line in (D) represents the theoretical back azimuth to Taal. The circles represent estimates from ray theory (Figure 7, Table 1). Note the increase in higher frequencies at around 12:00 UTC visible in B up to 2 Hz.

Figure 7: Infrasound propagation modeling results using G2S model specifications at 09:00 UTC on 12 January 2020. The transmission loss at 0.1 Hz is computed using a Parabolic Equation model. Spherical and cylindrical transmission loss are plotted as solid gray lines. The estimated loss at I39PW is 56.5 dB (re 1 km). Superimposed are eigenrays from Taal to I39PW (for ray parameters, see Table 1).

Figure 8: Vertical channel from the IMS auxiliary seismic station Tagaytay (TGY) ground velocity (a) and spectrogram (b). The vertical channel TGY also recorded a low

frequency signal (TA) that is consistent with the infrasound signals recorded at the I39PW station (c and d) and corresponds with the timing of the intense infrasound.

Figure 9: Seismic analysis of TGY seismic station. The top panel (A) is the vertical channel from the station. Panel B is the Root Mean Square (RMS) amplitude over 30 minute windows between 0.05-0.15 Hz for the time period for the TA signal in black and the red line is the average RMS calculation over the whole window. Panel C is the calculated reduced displacement (Dr) for the TA signal. Panel D is the calculated RSAM for the vertical channel of the station.

Figure 10: Time-domain array processing results for seismic array CMAR for the activity on 12 through 14 January 2020. Throughout this period, seismic P-waves are detected in the 0.7-1.8 Hz frequency band. The theoretical back azimuth is indicated by the dashed blue line. In addition to numerous short-lived transient events, a continuous tremor signal is detected between 12:00 UTC on 12 January and 00:00 UTC on 13 January.

Figure 11: Comparison of waveforms observed at TGY (top row; 11 km) and CMAR (bottom row; 2404 km). The time has been corrected for the P-wave propagation time toward the seismic station.

Figure 12: Summary of analysis and eruption phases during the 12 January 2020 eruption of Taal Volcano. Each phase transition is denoted with a vertical black line. Official reports of plume heights from Tokyo Volcanic Ash Advisory Center (VAAC) and Philippine Institute of Volcanology and Seismology (PHIVOLCS) are denoted by blue symbols (left axis). The black line plot shows plume heights determined from Himawari-8 satellite observations by Van Eaton et al. (2022) and the timing of discrete eruptive pulses are shown as black open circles (suggesting an unsteady eruption rate). Infrasound data (red line, left inset axis) shows acoustic power (watts at vent from I39PW); horizontal red dashed lines give time ranges of infrasound detections from other stations (noted in black on the left) and have been time corrected for atmospheric

propagation. Volcanic lightning (green line plot) shows total flashes per minute as a 5-minute running average (right axis). Seismic tremor signals are shown as horizontal lines as detected from stations TA (solid purple line) and TS (dashed purple line).

Figures

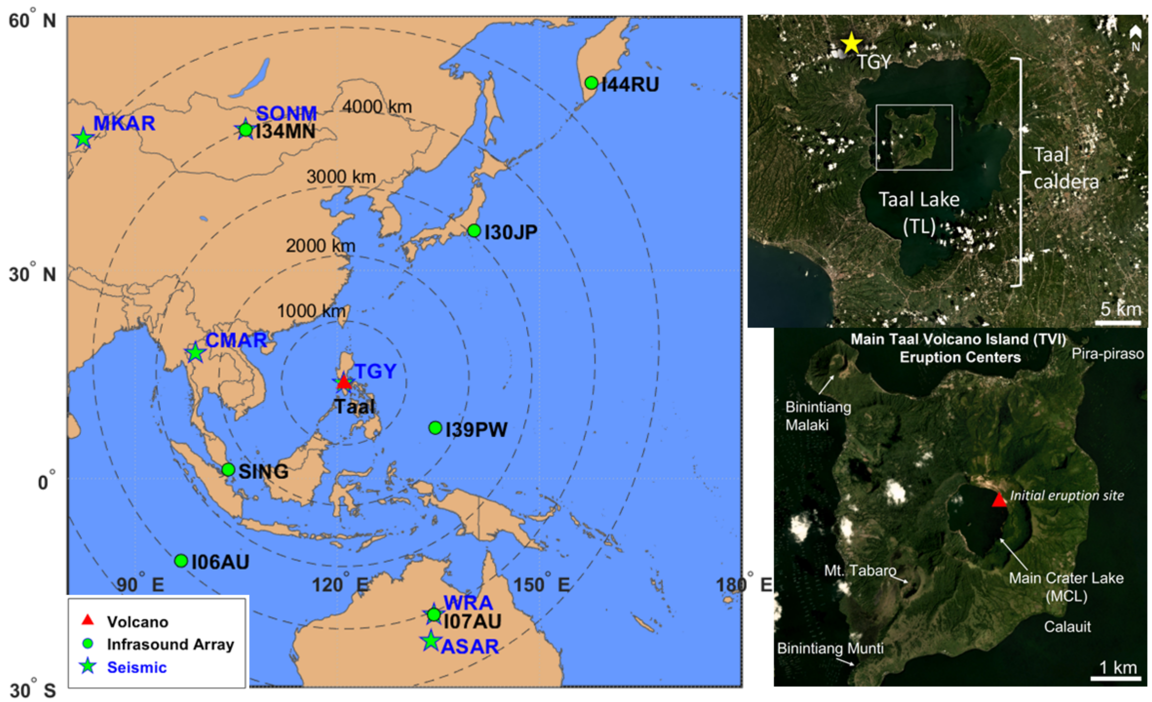

Figure 1: Regional map on the left, showing the remote network used in the study, and indicating infrasound arrays (circles), seismic arrays (stars), and distances from the volcano. On the right, volcano area map and annotated satellite images showing the Taal caldera, Volcano Island (TVI) in Taal Lake (TL), and features on the island, including the Main Crater Lake (MCL), and the initial eruption site. Modified from Global Volcanism Program, 2020. Imagery courtesy of Planet Inc.

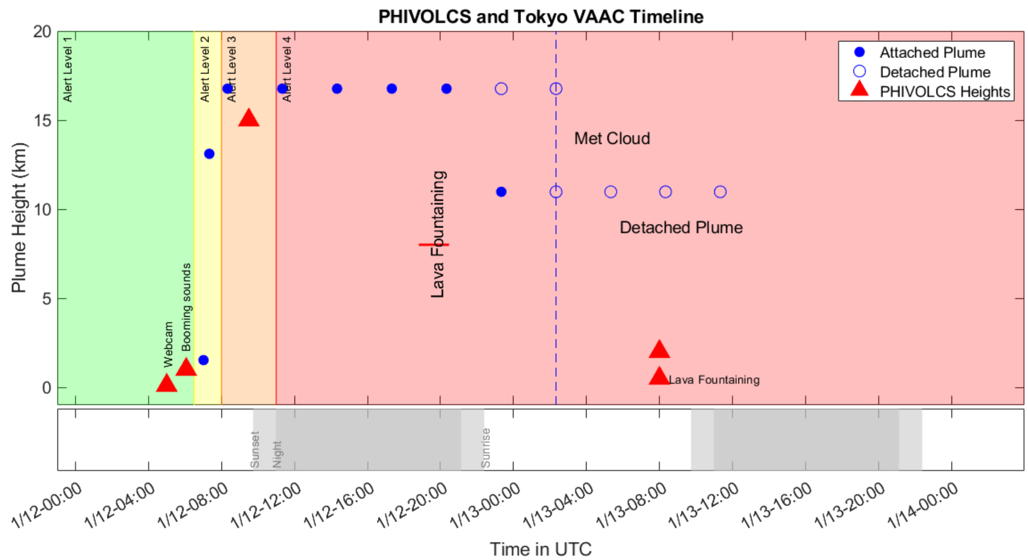

Figure 2: Timeline of Taal Volcano's climactic eruption 12–13 January 2020 from Philippine Institute of Volcanology and Seismology (PHIVOLCS) bulletin reports (red triangles) and Tokyo Volcanic Ash Advisory Center (VAAC) alerts (blue circles). Open circles indicate when the plume was reported as detached from the vent. Possible influence of meteorologic cloud cover was noted after the blue dashed line. The PHIVOLCS alert level is plotted as a colored background with Alert level 1 in green, 2 in yellow, 3 in orange, and 4 in red. Time frame of lava fountaining reported by PHIVOLCS is noted. Local day and night are also highlighted.

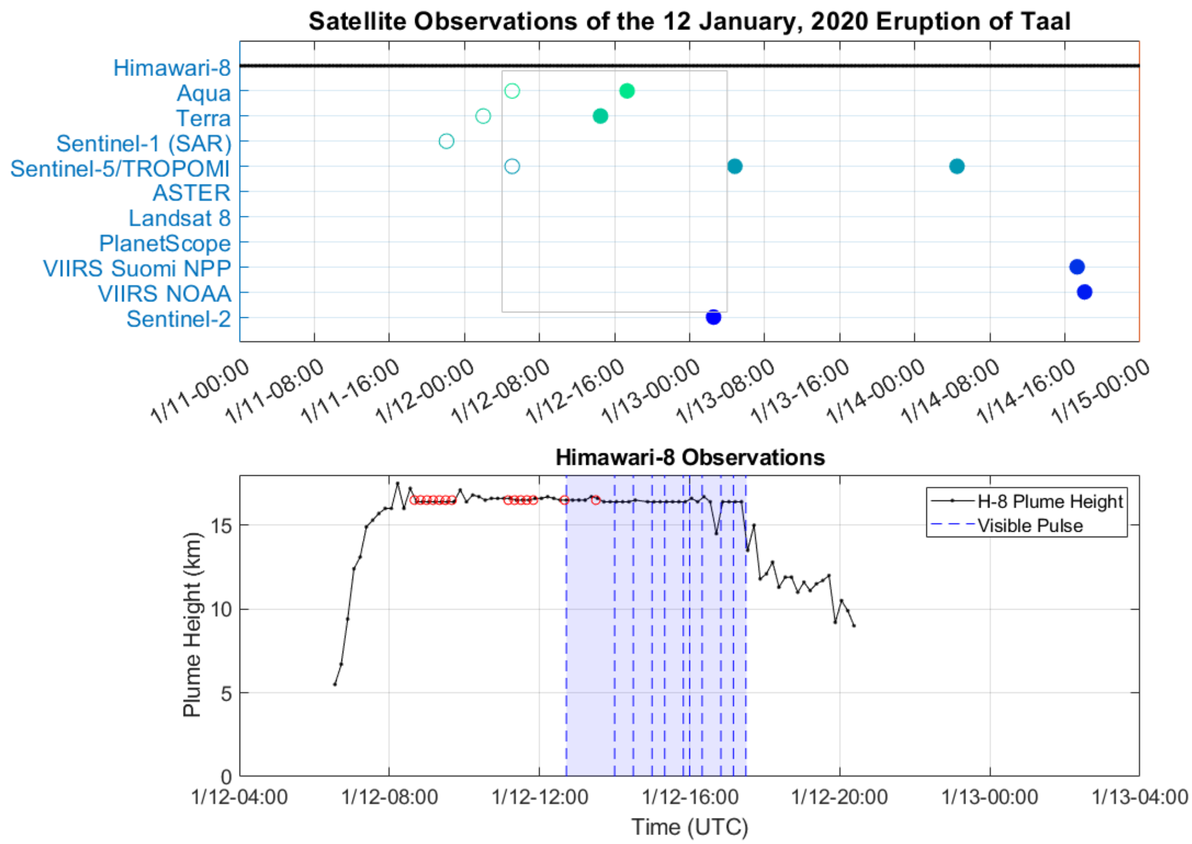

Figure 3: Top figure showing there was limited coverage by satellites; open circles are passes that actually cover the area of interest (crater of Taal Volcano) but didn't image the eruption. The Himawari-8 satellite, a geostationary meteorological satellite with a 10 minute repeat, provided the most coverage. Bottom figure showing the Himawari-8 plume height retrievals (in black), with red open circles indicating where the plume may actually be higher. The dashed blue lines indicate times when a pulsating plume can be seen in the Himawari-8 images.

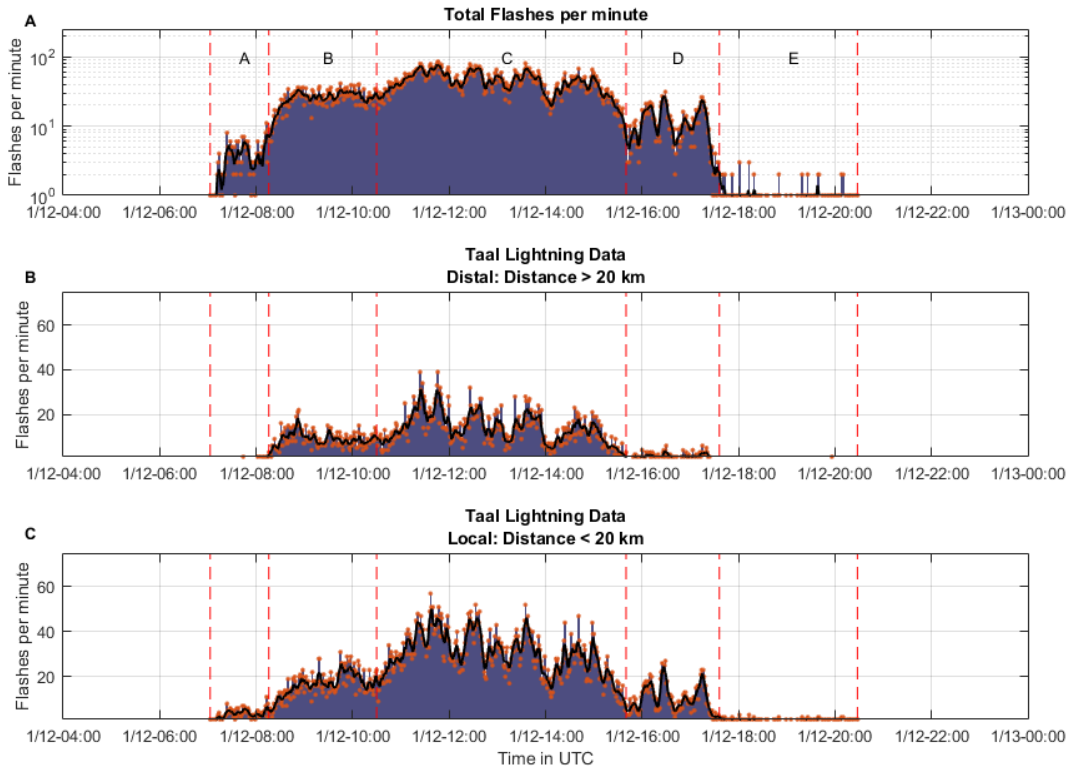

Figure 4: Rates of volcanic lightning produced by the Taal eruption plume as detected by the GLD360 network from Van Eaton et al. (2022). (A) rates of all lightning flashes within 200 km of the vent; (B) rates of distal lightning, defined by flashes occurring 20–200 km from vent; and (C) local lightning within 20 km of vent. Orange symbols give the per-minute flash rates and black line shows the 5-minute running average. Volcanic lightning was first detected at 07:03:02 UTC on 12 January 2020. The dataset was then visually divided into several stages of electrical activity (A-E) based on changes in the flash rate.

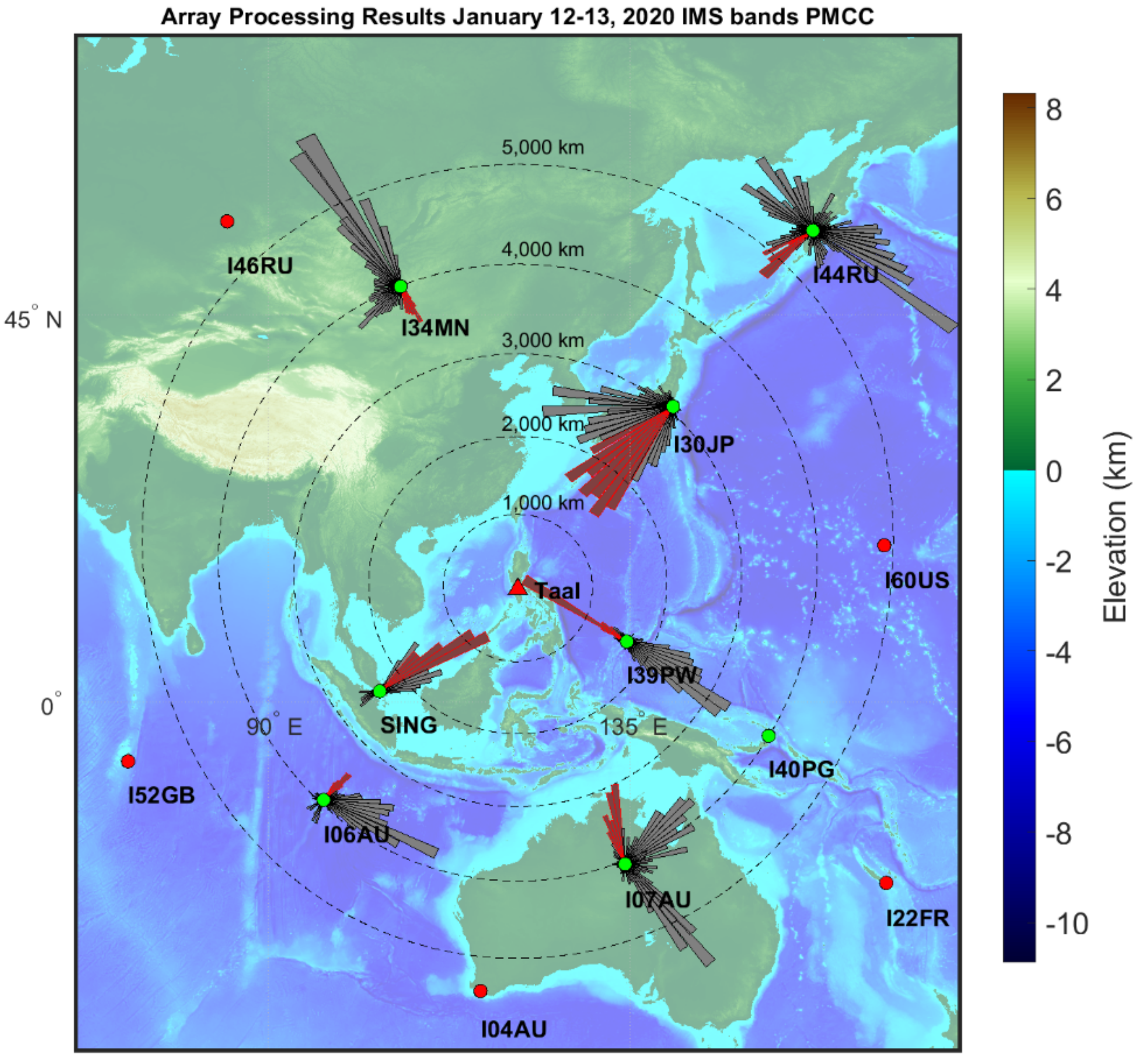

Figure 5: Summary of Progressive Multi-Channel Correlation (PMCC) results highlighting infrasound detections of the Taal eruption in red along with the background array processing results for each infrasound array in the region. The standard IMS array processing configuration was used. Stations are plotted in green (detection) or red (no detection), with the rose diagram of detections for 12 and 13 January 2020. Station I40PG had data quality issues and while the eruption was detected, the station does not have reliable array processing results. Results are inferred to be related to volcanic activity based on back azimuth and timing of detections.

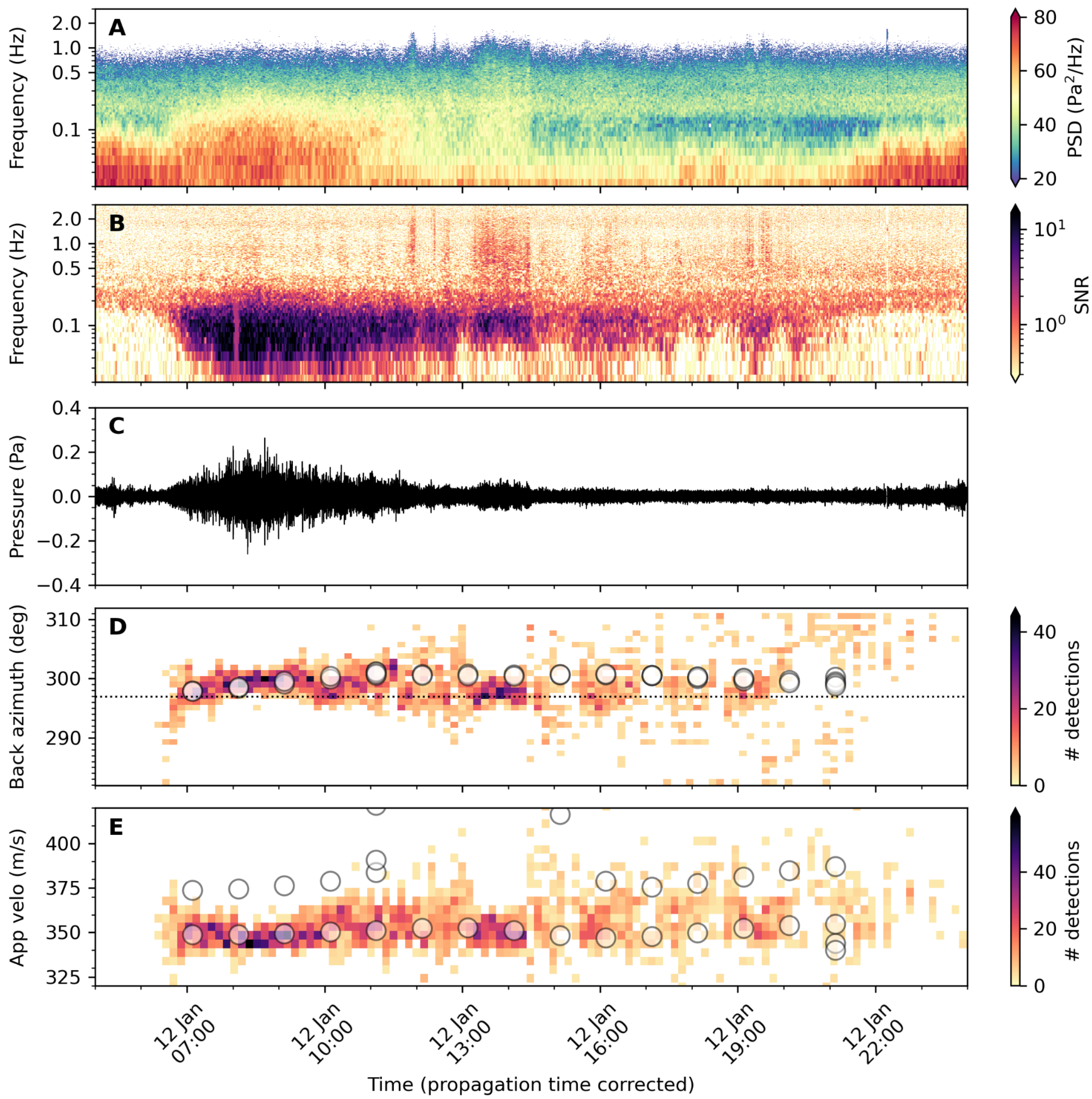

Figure 6: Analysis of infrasound signals from the I39PW array, focusing on the eruption of Taal Volcano on 12 January 2020. The results have been adjusted for a propagation time of 6322 seconds to relate infrasonic features to eruptive activity. The spectrograms (A, B) and best beam (C) have been computed using the slowness vector estimates obtained over the 0.07–1.0 Hz band. The dashed line in (D) represents the theoretical back azimuth to Taal. The circles represent estimates from ray theory (Figure 7, Table 1). Note the increase in higher frequencies at around 12:00 UTC visible in B up to 2 Hz.

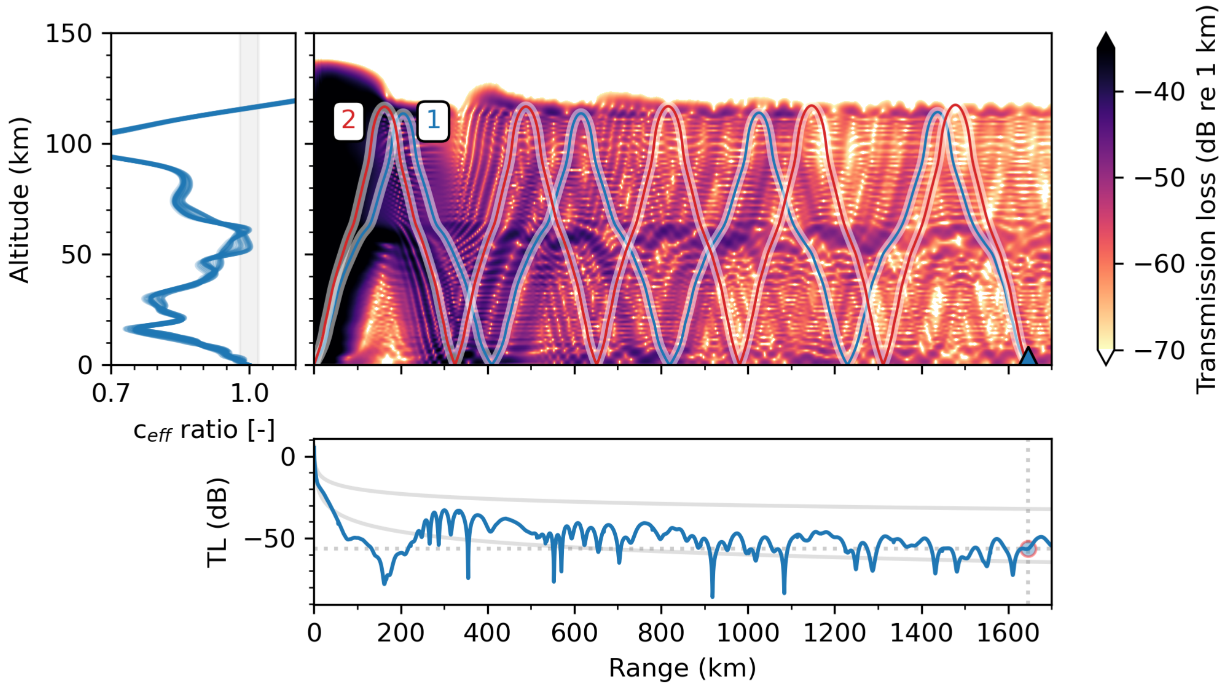

Figure 7: Infrasound propagation modeling results using G2S model specifications at 09:00 UTC on 12 January 2020. The transmission loss at 0.1 Hz is computed using a Parabolic Equation model. Spherical and cylindrical transmission loss are plotted as solid gray lines. The estimated loss at I39PW is 56.5 dB (re 1 km). Superimposed are eigenrays from Taal to I39PW (for ray parameters, see Table 1).

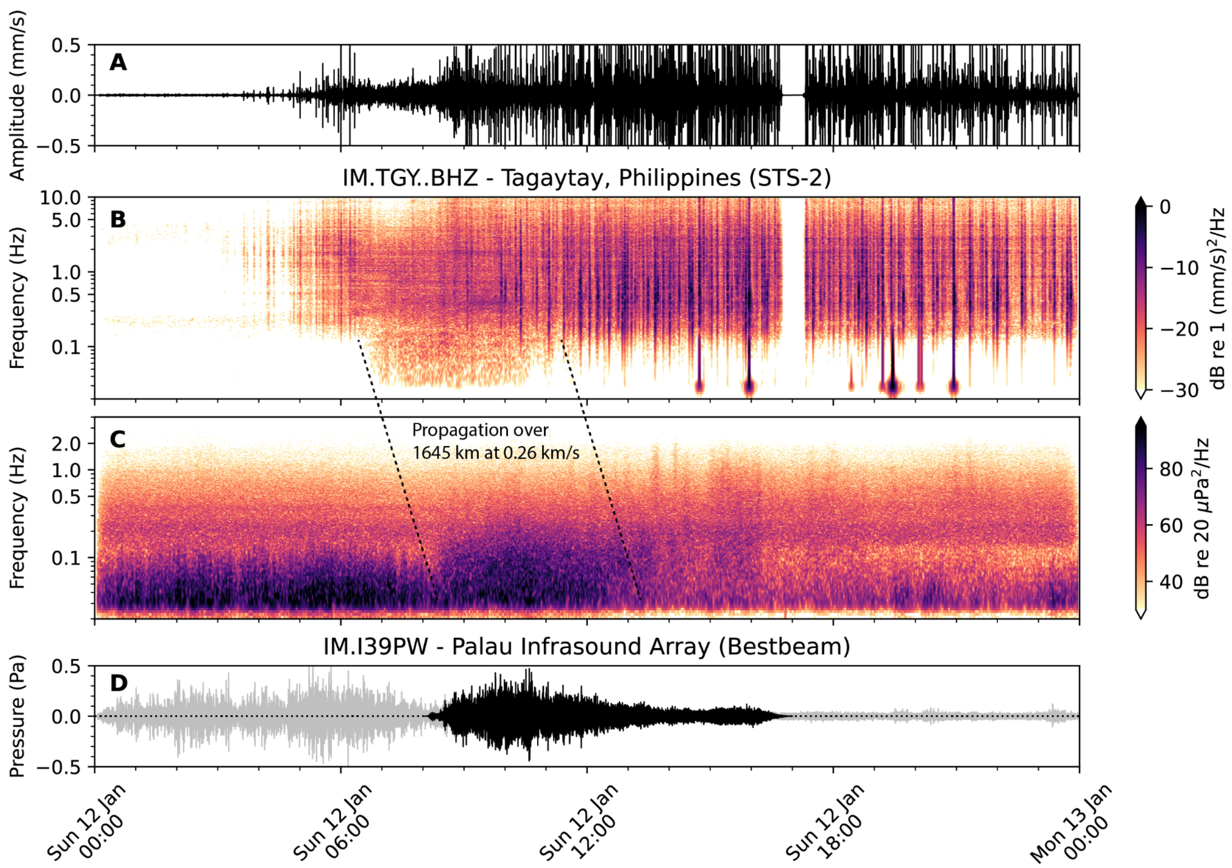

Figure 8: Vertical channel from the IMS auxiliary seismic station Tagaytay (TGY) ground velocity (a) and spectrogram (b). The vertical channel TGY also recorded a low frequency signal (TA) that is consistent with the infrasound signals recorded at the I39PW station (c and d) and corresponds with the timing of the intense infrasound.

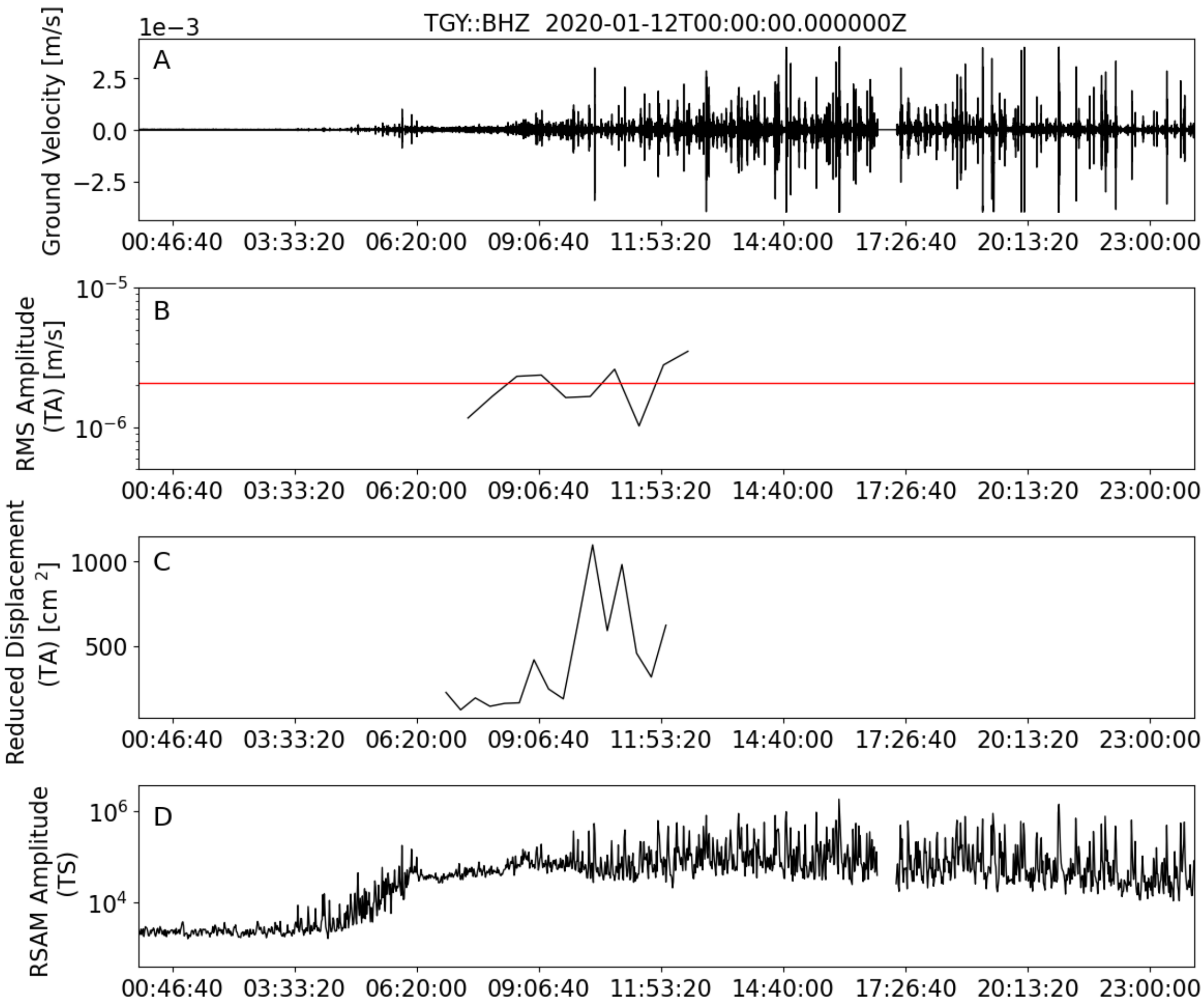

Figure 9: Seismic analysis of TGY seismic station. The top panel (A) is the vertical channel from the station. Panel B is the Root Mean Square (RMS) amplitude over 30 minute windows between 0.05-0.15 Hz for the time period for the TA signal in black and the red line is the average RMS calculation over the whole window. Panel C is the calculated reduced displacement (Dr) for the TA signal. Panel D is the calculated RSAM for the vertical channel of the station.

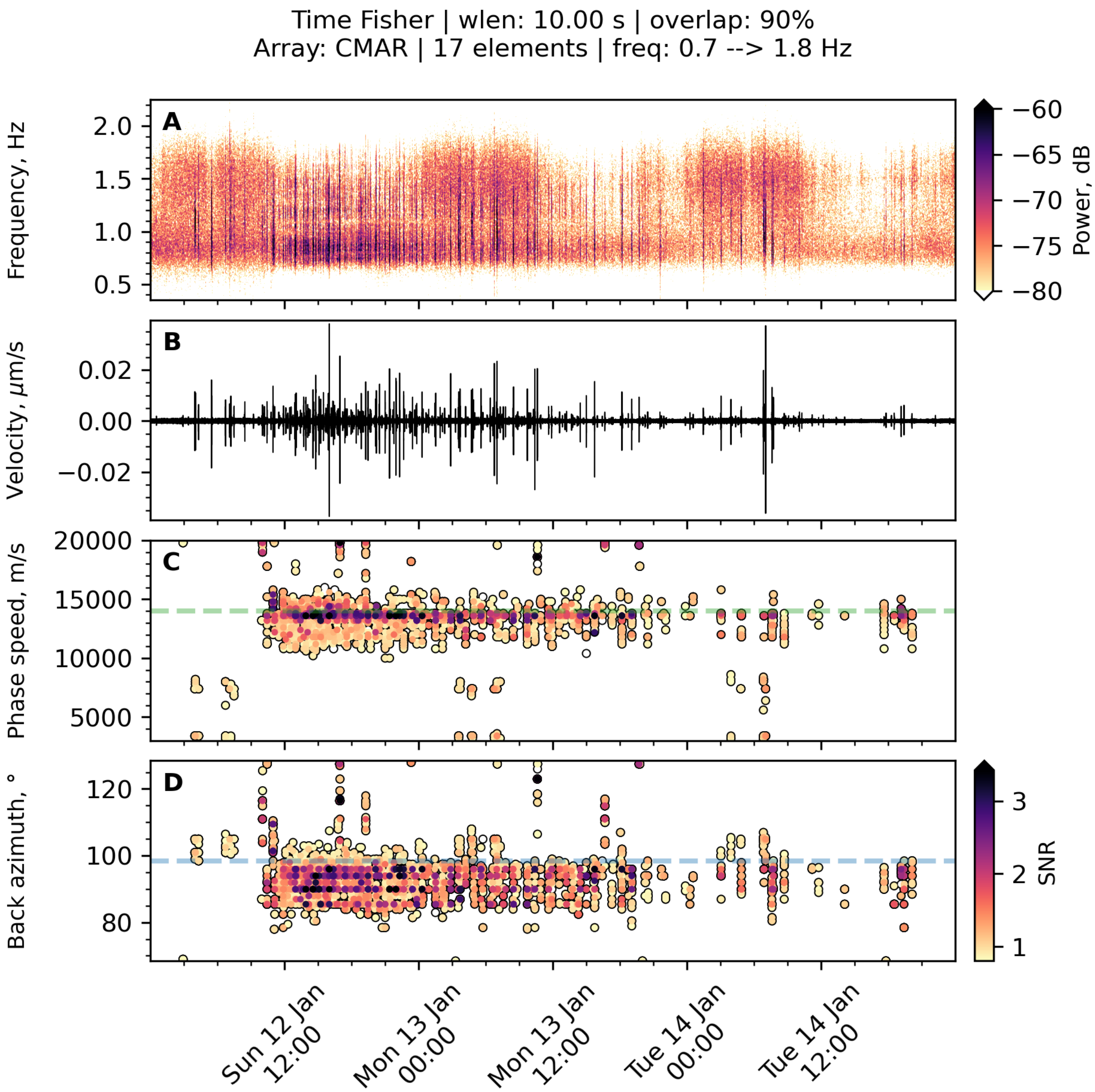

Figure 10: Time-domain array processing results for seismic array CMAR for the activity on 12 through 14 January 2020. Throughout this period, seismic P-waves are detected in the 0.7-1.8 Hz frequency band. The theoretical back azimuth is indicated by the dashed blue line. In addition to numerous short-lived transient events, a continuous tremor signal is detected between 12:00 UTC on 12 January and 00:00 UTC on 13 January.

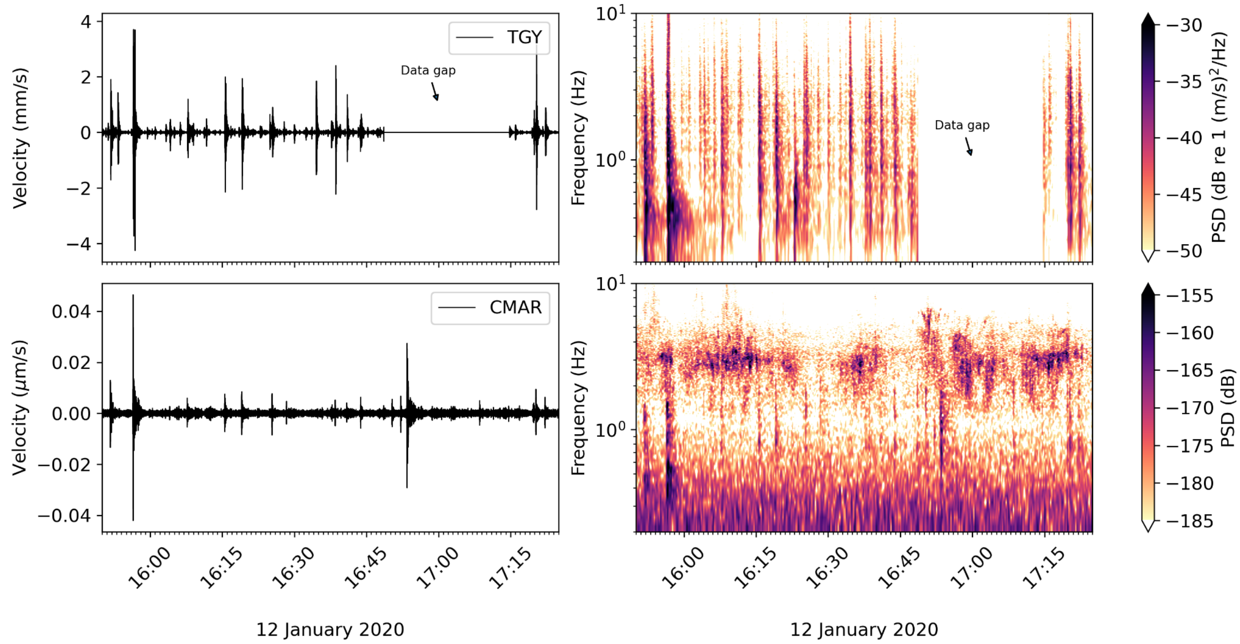

Figure 11: Comparison of waveforms observed at TGY (top row; 11 km) and CMAR (bottom row; 2404 km). The time has been corrected for the P-wave propagation time toward the seismic station.

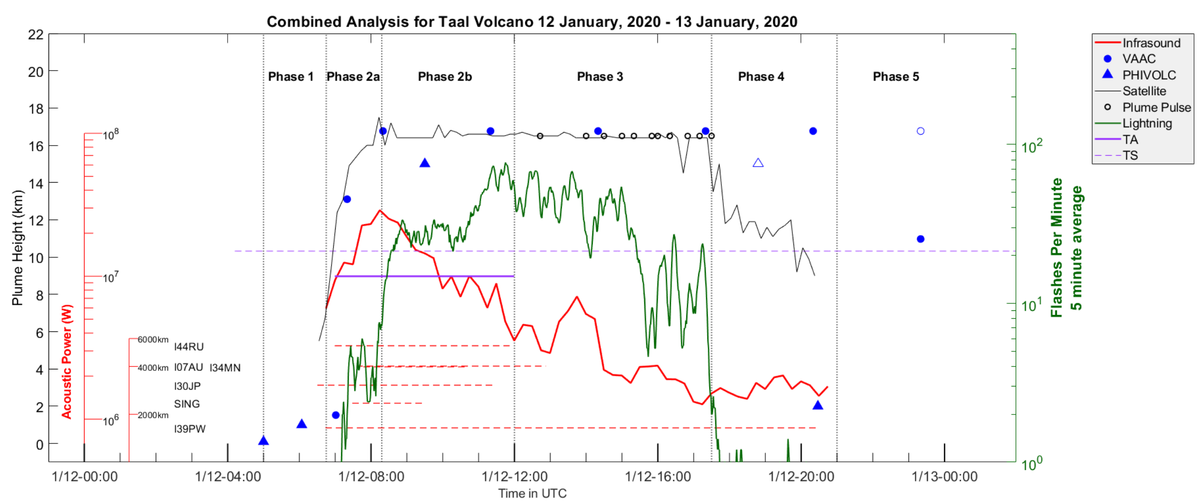

Figure 12: Summary of analysis and eruption phases during the 12 January 2020 eruption of Taal Volcano. Each phase transition is denoted with a vertical black line. Official reports of plume heights from Tokyo Volcanic Ash Advisory Center (VAAC) and Philippine Institute of Volcanology and Seismology (PHIVOLCS) are denoted by blue symbols (left axis). The black line plot shows plume heights determined from Himawari-

8 satellite observations by Van Eaton et al. (2022) and the timing of discrete eruptive pulses are shown as black open circles (suggesting an unsteady eruption rate). Infrasound data (red line, left inset axis) shows acoustic power (watts at vent from I39PW); horizontal red dashed lines give time ranges of infrasound detections from other stations (noted in black on the left) and have been time corrected for atmospheric propagation. Volcanic lightning (green line plot) shows total flashes per minute as a 5-minute running average (right axis). Seismic tremor signals are shown as horizontal lines as detected from stations TA (solid purple line) and TS (dashed purple line).